

# EXO SKRYER: A JAX-ACCELERATED SUB-STELLAR ATMOSPHERIC RETRIEVAL FRAMEWORK.

ELSPETH K.H. LEE

Center for Space and Habitability, University of Bern, Gesellschaftsstrasse 6, CH-3012 Bern, Switzerland  
Version February 24, 2026

## ABSTRACT

Contemporary exoplanet and brown dwarf atmospheric research relies heavily on retrieval frameworks to recover thermal and chemical properties and perform model comparison in an observational data-driven approach. However, the computational effort required for retrieval modelling has rapidly increased, driven by JWST data that covers large spectral intervals at moderate spectral resolutions, and ground-based, high-resolution spectroscopy. To help tackle the computational burden faced by contemporary retrieval requirements, I present a new sub-stellar atmosphere retrieval modelling framework, *Exo Skryer*, that utilises the JAX library for Python to enable scalable, computationally efficient forward modelling as well as posterior sampling. I present example retrievals for pre- and current JWST era observations for both transmission and emission spectra, finding consistent results to previous retrieval modelling efforts, apart from a WASP-107b test case. In addition, I present a new method to directly retrieve the real and imaginary optical constants ( $n$ ,  $k$ ) of suspected aerosol infrared absorption features. Due to its computational expediency, *Exo Skryer* will be highly suited for future demanding retrieval efforts that incorporate more spatial dimensionality, complex forward models and high-dimensional parameter sets.

*Subject headings:* planets and satellites: atmospheres – brown dwarfs – methods: numerical

## 1. INTRODUCTION

The information content of exoplanet and brown dwarf atmospheres available for analysis by astronomers has increased substantially since the start of the JWST era, with new insights into the nature of their atmospheres published on a near-weekly basis. In tandem with this slew of new data, retrieval modelling has now become a standard component of first-look analyses of new JWST data. Numerous retrieval codes have been developed in the past couple decades, with several listed in [MacDonald & Batalha \(2023\)](#).

The aim of retrieval in contemporary exoplanet atmospheric research is to statistically infer in a formal manner the atmospheric parameters of the exoplanet utilising a data-driven approach, where the observational data points and errors are used to inform the likelihood of a set of sampled forward model parameters in a statistically consistent approach. Model comparison can also be made in a systematic way through comparing the ratio of Bayesian evidence. This is performed by neglecting or adding parts of the forward model from an initial baseline, for example, removing individual gas phase opacity sources one-by-one (e.g. [Felix et al. 2025](#); [Welbanks et al. 2025](#)). More advanced model comparison techniques such as ‘leave one out’ (LOO) (e.g. [Welbanks et al. 2023](#)) to estimate the sensitivity of the results to individual data points, have also been applied to exoplanet retrieval efforts.

The high performance computing (HPC) infrastructure accessible to typical researchers in astrophysics is increasingly becoming more heterogeneous, including mixtures of central processing units (CPUs) and graphics processing units (GPUs). This is primarily driven by the rapid development and rollout schedules of machine learning (ML) products in the technology industrial sector, where GPUs are a critical component for scaling the training and inference for these models. Institute and national HPC infrastructures are increasingly trending with industry in procurement for their HPC inventories.

As both the research interest and utilisation of this infrastructure at research institutes increases, this is making GPUs more commonly available at institutional HPC centres. This is incentivising scientific codes to migrate from CPUs to GPUs, especially for computationally intensive workloads such as exoplanet atmosphere retrieval modelling.

In this paper, I present a new atmospheric retrieval framework, *Exo Skryer*, a flexible Python + JAX based code which can operate both the forward model and sampling scheme on CPUs, GPUs or a combination of both. I apply *Exo Skryer* to topical 1D transmission and emission spectra scenarios encountered by contemporary sub-stellar retrieval studies. This paper acts as the core reference for *Exo Skryer*, with further development expected to occur in the next years. In Section 2, I present the *Exo Skryer* retrieval framework, the JAX programming paradigm and nested-sampling options with JAX, the temperature-pressure, chemistry and cloud structure options within *Exo Skryer*. In Section 3, I detail the various gas phase opacities that *Exo Skryer* can utilise. In Section 4, I detail the radiative-transfer methodology used for the 1D transmission spectra retrievals. In Section 5, I detail the radiative-transfer methodology used for the 1D emission spectra retrievals. In Section 6, I present various retrieval examples and results using *Exo Skryer*, spanning pre-JWST and JWST era observational data. Section 7 contains the discussion, and Section 8 the conclusions of this study.

## 2. THE EXO SKRYER FRAMEWORK

*Exo Skryer* is designed with high modularity and flexibility in mind. The code is driven by a simple YAML-formatted input file, which details the physics modules, opacity sources, retrieval parameters, sampling options and runtime environment. *Exo Skryer* then uses the configuration to build a custom forward model that is then used for the likelihood evaluation inside the sampling framework. This same YAML file is then used to post-process the posterior samples to produce corner plots, best fit plots and other diagnostics, ensuring the exact same custom forward model is used. Parameters and

any intermediate data are stored as flexible Python dictionaries, which allows data present in the YAML file to be sent to the forward model building routine. This includes the sampled parameters, constant parameters and other auxiliary data that is required for the specific forward models to be used. Users can design and integrate their own JAX-compatible physics functions, such as radiative-transfer, chemistry and cloud models, which can be used to build the sampled forward model function.

### 2.1. Why JAX?

*Exo Skryer* is built around JAX, an open-source numerical computing library for Python that provides a NumPy-like interface with just-in-time compilation and accelerator support. Retrieval workflows are dominated by repeated forward-model evaluations inside a sampler; even modest improvements in model throughput translate directly into substantial reductions in end-to-end runtime.

JAX offers three advantages that align well with retrieval modelling: (i) compilation of array-based kernels, reducing Python overhead and improving throughput; (ii) straightforward execution on CPUs and GPUs, enabling scalable evaluation over large spectral grids; and (iii) automatic differentiation, which provides a pathway to future gradient-based optimisation and inference, as well as sensitivity analyses.

The main trade-off is that JAX encourages a more functional programming style and requires care with side effects and control flow, which can necessitate refactoring and additional testing. In return, it provides a robust foundation for efficient retrieval modelling on increasingly heterogeneous HPC infrastructure.

### 2.2. Nested sampling with JAX

Nested sampling (NS) (e.g. Skilling 2004; Buchner 2023) has become the de facto standard sampling technique for sub-stellar atmosphere retrieval modelling in the past decade (e.g. Welbanks & Madhusudhan 2021), mostly outpacing the MCMC based techniques used in earlier retrieval efforts (e.g. Benneke & Seager 2012) in day-to-day workloads. An in-depth description of NS is not in the scope of this study, however, a key benefit of NS is the ability to easily make model comparison and detection significance through calculation of the ‘Bayes evidence’ of different relative parameter sets.

I use three nested sampling frameworks in *Exo Skryer*: *pymultinest* (Buchner et al. 2014), *dynesty* (Speagle 2020) and *JAXNS* (Albert 2020). *JAXNS* can operate on the GPU, enabling both the sampling and forward model stages to be performed on the GPU. *pymultinest* and *dynesty* cannot utilise the GPU at the sampling stage, but benefit instead from the JAX forward model, which is able to be performed on the GPU, or multi-threaded CPU. This enables a hybrid approach similar to the *BeAR* retrieval model (Kitzmann et al. 2020), where the sampling stage is performed on the CPU, with each likelihood evaluation performed on the GPU. In addition, the JAX infrastructure also accelerates CPU only workloads, with *Exo Skryer* able to run without the need for GPUs. This allows practitioners without GPU access to also run performant retrievals. The only other JAX based retrieval model applied to exoplanet and brown dwarf atmospheres that I am aware of at this time is *ExoJAX* (Kawahara et al. 2022, 2025).

#### 2.2.1. Speed testing samplers

TABLE 1  
RETRIEVAL COMPLETION TIME (MINUTES) FOR THE DIFFERENT NESTED SAMPLING OPTIONS IN *Exo Skryer* FOR THE HD 209458B PRE-JWST RETRIEVAL EXAMPLE.

Scheme	ck ( $R=1000$ )	OS ( $R=10,000$ )	OS ( $R=20,000$ )
<i>pymultinest</i>	23	18	28
<i>dynesty</i>	63	40	66
<i>JAXNS</i>	324	252	421

To compare the computational efficiency of a nominal setup of *Exo Skryer*, I performed the HD 209458b pre-JWST retrieval setup (11 parameters) from Section 6.1 with *pymultinest*, *dynesty* and *JAXNS* utilising the same JAX forward model setup, each using ck at  $R = 1,000$  and OS at  $R = 10,000$  and  $R = 20,000$ . 1000 live-points and a stopping criterion of  $\Delta \log Z = 0.1$  were used in all cases. Table 1 presents the results of this test, where *pymultinest* is the most efficient and *JAXNS* the least efficient.

For the *JAXNS* test, a plausible explanation is that the consumer-grade GPU used in this study (Nvidia RTX 4090) may be too saturated performing the sampling as well as the forward model, which significantly degrades performance. Owing to this speed testing and recommendations from previous comparison studies (e.g. Speagle 2020), I use *dynesty* for all retrieval models in this study.

### 2.3. Likelihood

I use a standard independent Gaussian errors formulation for the log-likelihood function (e.g. Kitzmann et al. 2020)

$$\log \mathcal{L} = \sum_{i=1}^N \left[ -\log \sigma_{\text{eff},i} - \frac{1}{2} \log(2\pi) - \frac{1}{2} \left( \frac{r_i}{\sigma_{\text{eff},i}} \right)^2 \right], \quad (1)$$

where  $r_i$  is the residual between the observational data and forward model for the  $i$ th observational point

$$r_i = y_i^{\text{obs}} - y_i^{\text{model}}, \quad (2)$$

and  $\sigma_{\text{eff}}$  the effective  $1\sigma$  errors in the observational point. Any invalid outputs from the forward model are discarded with a log-likelihood of  $\log \mathcal{L} = -10^{300}$ .

For brown dwarf retrievals, I include an error inflation parameter,  $c$ , in the form

$$\sigma_{\text{eff}}^2 = \sigma^2 + 10^{2c}, \quad (3)$$

with the prior bounds (e.g. Burningham et al. 2017)

$$\log_{10} [0.1 \times \min(\sigma)] < c < \log_{10} [10 \times \max(\sigma)], \quad (4)$$

where  $\sigma$  is the  $1\sigma$  uncertainty in the observational data. For retrievals that don’t require inflation, I force  $c = -99$ , effectively setting zero error inflation.

### 2.4. T-p profile parametrisation

Every retrieval framework must offer a simple parametrisation of the T-p profile that is quick to evaluate, and provides the first step in performing the forward model. Below I present some options available in *Exo Skryer* used in the current study.

#### 2.4.1. Isothermal

The simplest T-p profile, and commonly used in transmission spectra retrieval efforts, is assuming the entire atmosphere is isothermal throughout the vertical extent. This leads to only  $T_{\text{iso}}$  [K] as the retrieved variable for this structure

$$T(p) = T_{\text{iso}}. \quad (5)$$

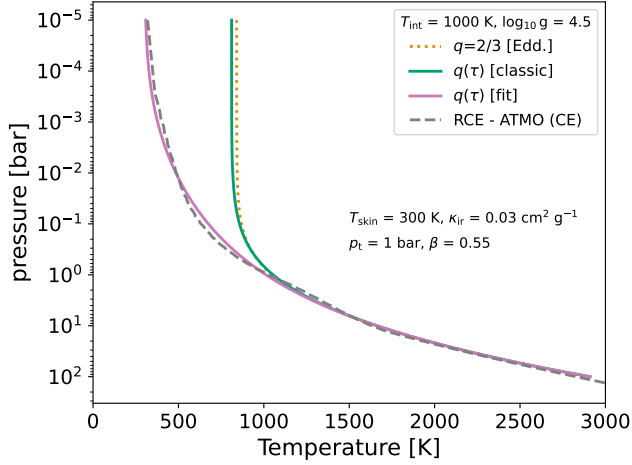


Fig. 1.— Example of the modified Milne T-p profile scheme for brown dwarf retrievals in Sect. 2.4.3 (purple, solid), compared to the original Milne profile (orange, dotted), classic Hopf solution (green, solid) and a chemical equilibrium ATMO profile (grey, dashed) from Phillips et al. (2020). The bulk parameters are  $T_{\text{int}} = 1000$  K,  $\log_{10} g = 4.5$ , with the modified Milne profile parameters printed inside the figure.

I use this profile in the WASP-17b transmission spectra retrieval in Section 6.3.

#### 2.4.2. Barstow 2020

A simple, but more physical option was used in Barstow (2020), where a ‘stratospheric’ isothermal temperature,  $T_{\text{strat}}$  [K], is chosen with an adiabatic profile between 0.1-1 bar, and then an isothermal deep pressure region

$$T(p) = \begin{cases} T_{\text{strat}}, & p \leq 0.1, \\ T_{\text{strat}} \left(\frac{p}{0.1}\right)^{\kappa}, & 0.1 < p < 1, \\ T_{\text{strat}} \left(\frac{1}{0.1}\right)^{\kappa}, & p \geq 1, \end{cases} \quad (6)$$

where  $\kappa \approx 2/7$  is the adiabatic constant. Again, only a single parameter,  $T_{\text{strat}}$  [K], is required in the retrieval model. I use this profile in the HD 209458b pre-JWST transmission spectra retrieval setup in Section 6.1.

#### 2.4.3. Modified Milne

For isolated exoplanet and brown dwarf atmospheres, due to the lack of irradiation, the T-p structure is expected to be more monotonic and driven primarily by the internal temperature. An option is to use the classic grey Milne analytical radiative-equilibrium (RE) solution

$$T^4(\tau) = \frac{3}{4} T_{\text{int}}^4 [\tau + q(\tau)], \quad (7)$$

where  $q(\tau)$  is the Hopf function, which is  $q(\tau) = 2/3$  when taking the Eddington approximation for isotropic, diffuse emission. The optical depth,  $\tau$ , of the grey atmosphere is given by

$$\tau(p) = \frac{\kappa_{\text{ir}}}{g} p, \quad (8)$$

where  $\kappa_{\text{ir}}$  [ $\text{cm}^2 \text{g}^{-1}$ ] is the constant infrared band opacity of the atmosphere,  $p$  [dyne] the atmospheric pressure and  $g$  [ $\text{cm s}^{-2}$ ] the gravitational acceleration.

For retrieval purposes, I propose a parametrised Hopf function that takes the form of a stretched exponential function,

$$q(\tau) = q_{\infty} + (q_0 - q_{\infty}) \exp \left[ - \left( \frac{\tau}{\tau_t} \right)^{\beta} \right], \quad (9)$$

which can be transposed to pressure coordinates when  $\kappa_{\text{ir}}$  is constant

$$q(p) = q_{\infty} + (q_0 - q_{\infty}) \exp \left[ - \left( \frac{p}{p_t} \right)^{\beta} \right], \quad (10)$$

where  $q_0$  is the value of  $q$  as  $\tau \rightarrow 0$ ,  $q_{\infty}$  the value of  $q$  as  $\tau \rightarrow \infty$ ,  $p_t$  [dyne] the transition pressure and  $\beta$  a stretching parameter. Physically,  $\tau_t$  or  $p_t$  marks the approximate boundary between the deep and upper  $q$  dominance and  $\beta$  controls the sharpness of the transition, with  $\beta > 1$  being stronger and  $\beta < 1$  being weaker than an exponential transition respectively. The parameter  $q_0$  is related to the skin temperature of the atmosphere through

$$q_0 = \frac{4}{3} \left( \frac{T_{\text{skin}}}{T_{\text{int}}} \right)^4, \quad (11)$$

a suitable retrieval parameter is then the skin to internal temperature ratio,  $T_{\text{ratio}}$  (0,1),

$$T_{\text{ratio}} = \frac{T_{\text{skin}}}{T_{\text{int}}}. \quad (12)$$

Here, a possibility is to use the classic grey atmosphere solutions at  $\tau = \infty$  ( $q_{\infty} \approx 0.71$ ) and  $\tau = 0$  ( $q_0 \approx 1/\sqrt{3}$ ) (e.g. Mihalas 1978). However, this classic solution was found in Kitzmann et al. (2020) to not be flexible enough for general brown dwarf retrieval modelling. I therefore relax constraints on  $q_0$  to allow greater flexibility in the T-p structure, and the ability to recover a T-p profile more akin to non-grey RCE simulation results.

In Figure 1, I show an example fit to an ATMO (Phillips et al. 2020) RCE profile using this scheme, as well as the Eddington and classic Hopf function solution T-p profiles. The modified Milne scheme is able to well capture the T-p structure of the RCE model output, while the classic solutions turn off into an isothermal upper atmosphere too quickly, and fail to capture the decreasing temperature gradient from the RCE model. The modified Milne profile is not as flexible as the piecewise polynomial or spline schemes that have been used in past brown dwarf retrieval studies (e.g. Line et al. 2015; Kitzmann et al. 2020; Kothari et al. 2024), but offers a useful option for direct comparison to forward RCE model results. Overall, the required retrieval parameters for this scheme are  $T_{\text{int}}$  [K],  $\kappa_{\text{ir}}$  [ $\text{cm}^2 \text{g}^{-1}$ ],  $T_{\text{ratio}}$ ,  $p_t$  [dyne] and  $\beta$  for five total. I use this T-p profile for the Gliese 229B retrieval in Section 6.5.

#### 2.4.4. Modified Guillot

A commonly utilised T-p profile parametrisation for hot Jupiters are the several radiative-equilibrium (RE), semi-grey analytical solutions derived in Guillot (2010). The main T-p solution in Guillot (2010) is given by

$$T^4(\tau) = \frac{3T_{\text{int}}^4}{4} \left[ \frac{2}{3} + \tau \right] + \frac{3T_{\text{irr}}^4}{4} \mu_{\star} \left[ \frac{2}{3} + \frac{\mu_{\star}}{\gamma_{\text{v}}} + \left( \frac{\gamma_{\text{v}}}{3\mu_{\star}} - \frac{\mu_{\star}}{\gamma_{\text{v}}} \right) e^{-\gamma_{\text{v}}\tau/\mu_{\star}} \right], \quad (13)$$

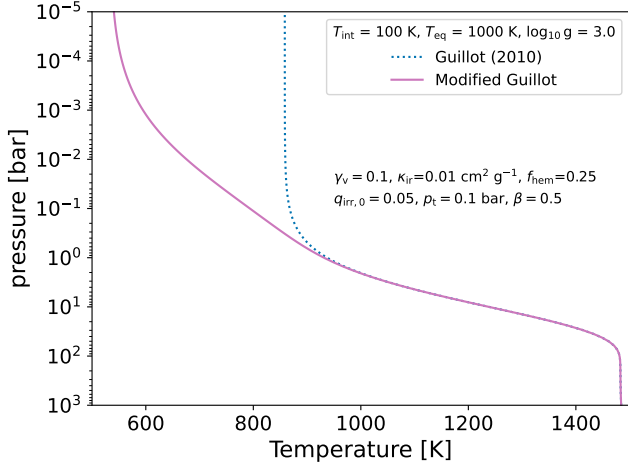


Fig. 2.— Example of the modified Guillot T-p profile scheme for hot Jupiter retrievals in Sect. 2.4.4 (purple, solid), compared to the original Guillot (2010) profile (blue, dotted). The bulk parameters are  $T_{\text{int}} = 100$  K,  $T_{\text{eq}} = 1000$  K,  $\log_{10} g = 3.0$ , with the modified Guillot profile parameters printed inside the figure.

where  $T_{\text{int}}$  [K] is the internal temperature,  $T_{\text{irr}}$  [K] the irradiation temperature,  $\gamma_v$  the ratio between the visible and infrared grey opacity and  $\mu_*$  the stellar zenith angle.

However, the Guillot (2010) profile tends toward an isothermal limit at small optical depth under the semi-grey, constant-opacity assumptions. This isothermal behaviour has been shown, when used in retrieval and T-p recovery contexts, to produce potentially unreliable results (e.g. Blecic, Dobbs-Dixon & Greene 2017; Barstow & Heng 2020; Dobbs-Dixon & Blecic 2022). Following a similar idea to the modified Milne profile in Section 2.4.3, I propose modifying the Guillot profile utilising a flexible Hopf-like function. Where, for a global mean T-p profile, I assume  $\mu_* = 1/\sqrt{3}$  and

$$T^4(\tau) = \frac{3T_{\text{int}}^4}{4} [q_{\text{int}}(\tau) + \tau] + \frac{3T_{\text{eq}}^4}{4} 4f_{\text{hem}} \left[ q_{\text{irr}}(\tau) + \frac{1}{\gamma_v \sqrt{3}} + \left( \frac{\gamma_v}{\sqrt{3}} - \frac{1}{\gamma_v \sqrt{3}} \right) e^{-\gamma_v \tau \sqrt{3}} \right], \quad (14)$$

where  $q_{\text{int}}$  is the parametrised Hopf function for the internal radiation, and  $q_{\text{irr}}$  the parametrised Hopf function for the incident radiation, where both use the stretched exponential form in Eq. (9).  $f_{\text{hem}} [0, 1]$  is the hemispheric energy redistribution factor (e.g. Guillot 2010), which typically takes values of 1 (sub-stellar point), 0.5 (dayside redistribution), and 0.25 ( $4\pi$  hemisphere redistribution). In this study, I assume a constant  $f_{\text{hem}} = 0.25$ .

Since for hot Jupiters  $T_{\text{eq}}^4 \gg T_{\text{int}}^4$ , the influence of the internal flux Hopf function is small and  $q_{\text{int}}$  can be returned to the Eddington approximation,  $q_{\text{int}} = 2/3$ , lowering the number of overall retrieved parameters. The irradiated flux Hopf function has the most impact on the modified Guillot T-p profile. For recovering suitable retrieval parameters, I forgo relating  $q_{\text{irr},0}$  to the skin temperature as in the modified Milne profile, instead directly retrieving  $0 < q_{\text{irr},0} \leq 2/3$  and setting  $q_{\text{irr},\infty} = 2/3$ . In Figure 2, I show an example of this modified T-p parametrisation, which shows the added upper atmosphere flexibility of this scheme compared to the original Guillot (2010) formulation. Overall, the required retrieval pa-

rameters for this scheme are  $T_{\text{int}}$  [K],  $T_{\text{eq}}$  [K],  $\kappa_{\text{ir}}$  [ $\text{cm}^2 \text{g}^{-1}$ ],  $\gamma_v$ ,  $q_{\text{irr},0}$ ,  $p_c$  [dyne] and  $\beta$  for seven total if  $f_{\text{hem}}$  is kept fixed.

I note that these additional parametrisations break the RE solution presented in Guillot (2010), similar to the modified Milne profile, and so retrieved profiles should use caution when physically interpreting parameters derived from retrievals. However, this parametrisation offers a more flexible, retrieval-friendly generalisation of the Guillot profile that can emulate non-grey upper-atmosphere behaviour while retaining the deep-atmosphere RE solution. I use this profile for the HD 189733b dayside emission spectra retrieval in Section 6.4.

#### 2.4.5. Madhusudhan & Seager (2009)

The last T-p parametrisation I use in this study is the commonly applied Madhusudhan & Seager (2009) profile. This uses three main pressure nodes,  $p_0$  [dyne],  $p_1$  [dyne] and  $p_2$  [dyne], an upper reference temperature  $T_0$  [K] and two gradient parameters  $\alpha_1$  [ $\text{K}^{-1/2}$ ] and  $\alpha_2$  [ $\text{K}^{-1/2}$ ]. The T-p profile is generated using the following form (e.g. Pinhas et al. 2018; MacDonald 2023)

$$T(p) = \begin{cases} T_0 + \left( \frac{\ln(p/p_0)}{\alpha_1} \right)^2, & p_0 < p < p_1, \\ T_2 + \left( \frac{\ln(p/p_1)}{\alpha_2} \right)^2, & p_1 < p < p_2, \\ T_2 + \left( \frac{\ln(p_2/p_1)}{\alpha_2} \right)^2, & p > p_2, \end{cases} \quad (15)$$

where  $T_2$  [K] and  $p_2$  [dyne] are found through continuity of T-p through the atmosphere. This scheme is highly flexible, allowing upper atmosphere inversion behaviour as well as complex T-p gradients. I use this profile for the WASP-107b transmission spectra in Section 6.2.

### 2.5. Non-grey aerosol opacity

Including the effects of haze and cloud (aerosol) opacity in a parametrised manner that is also physically interpretable is a key goal of contemporary retrieval modelling efforts. Below, I detail the cloud models used in this study, focusing on non-grey formulations.

#### 2.5.1. Vertical cloud profiles

In *Exo Skryer*, the basic unit for the vertical cloud structures is the mass mixing ratio,  $q_c$  [ $\text{g g}^{-1}$ ], of the condensate

$$q_c = \frac{\rho_c}{\rho_a}, \quad (16)$$

where  $\rho_c$  [ $\text{g cm}^{-3}$ ] is the mass density of the condensate and  $\rho_a$  [ $\text{g cm}^{-3}$ ] the mass density of the background atmosphere. I use three schemes in this study: a vertically uniform slab profile across the entire vertical extent

$$q_c(p) = q_{c,\text{slab}}, \quad (17)$$

with only one parameter:  $q_{c,\text{slab}}$  [ $\text{g g}^{-1}$ ], a uniform slab defined between a top pressure and a given pressure range (e.g. Mullens, Lewis & MacDonald 2024)

$$q_c(p) = \begin{cases} 0, & p < p_{c,\text{top}}, \\ q_{c,\text{slab}}, & p_{c,\text{top}} \leq p \leq p_{c,\text{top}} + \Delta p, \\ 0, & p > p_{c,\text{top}} + \Delta p, \end{cases} \quad (18)$$

which has three parameters:  $q_{c,\text{slab}}$  [ $\text{g g}^{-1}$ ],  $p_{c,\text{top}}$  [dyne] and  $\Delta p$  [dyne], and a vertical mass mixing ratio profile with a base value,  $q_{c,\text{base}}$  [ $\text{g g}^{-1}$ ], given at a cloud base pressure,  $p_{c,\text{base}}$  [dyne], and a power law relation,  $\alpha$ , that reduces the mass mixing ratio with fractions of the pressure scale height

$$q_c(p) = q_{c,\text{base}} \left( \frac{p}{p_{c,\text{base}}} \right)^\alpha, \quad (19)$$

where  $q_c(p) = 0$  for  $p > p_{c,\text{base}}$ . This mimics the cloud structures typically seen in forward modelling efforts (e.g. [Ackerman & Marley 2001](#); [Ohno & Okuzumi 2017](#); [Batalha et al. 2026](#)) and has a total of three parameters:  $q_{c,\text{base}}$  [ $\text{g g}^{-1}$ ],  $p_{c,\text{base}}$  [dyne] and  $\alpha$ .

### 2.5.2. Fisher & Heng (2018)

[Fisher & Heng \(2018\)](#) propose a non-grey parametrisation of the cloud extinction opacity,  $\kappa_{c,\text{ext}}$  [ $\text{cm}^2 \text{g}^{-1}$ ], as

$$\kappa_{c,\text{ext}} = \frac{\kappa_0}{Q_0 x^{-a} + x^{0.2}}, \quad (20)$$

where  $\kappa_0$  [ $\text{cm}^2 \text{g}^{-1}$ ] is an effective baseline grey cloud opacity,  $Q_0$  related to the peak of the extinction efficiency curve,  $a$  a spectral slope index, and  $x = 2\pi r/\lambda$  the size parameter. The retrieved parameters for this scheme are therefore  $\kappa_0$  [ $\text{cm}^2 \text{g}^{-1}$ ],  $Q_0$ ,  $r$  [cm], and  $a$ . This formulation was compared to other cloud opacity schemes in [Barstow \(2020\)](#).

I propose a slight variant on the [Fisher & Heng \(2018\)](#) formulation to recover a more physically interpretable unit than the baseline cloud opacity. First, I use the equation for the cloud number density for a monodisperse size distribution, assuming spherical particles

$$N_0 = \frac{3\rho_a q_c}{4\pi\rho_d r_{\text{eff}}^3}, \quad (21)$$

where  $q_c$  [ $\text{g g}^{-1}$ ] is the mass mixing ratio of the cloud particles,  $\rho_a$  [ $\text{g cm}^{-3}$ ] the density of the background atmosphere,  $r_{\text{eff}}$  [cm] the effective particle size, and  $\rho_d$  [ $\text{g cm}^{-3}$ ] the bulk density of the cloud material. The opacity of the cloud particles is then approximated by

$$\kappa_{c,\text{ext}} \approx \frac{N_0 Q_{\text{ext}}(r_{\text{eff}}) \pi r_{\text{eff}}^2}{\rho_a} = \frac{3q_c Q_{\text{ext}}(r_{\text{eff}})}{4\rho_d r_{\text{eff}}}, \quad (22)$$

where, for convenience and computational expediency, the same fitting form to [Kitzmann & Heng \(2018\)](#) for  $Q_{\text{ext}}$  can be assumed

$$Q_{\text{ext}} = \frac{Q_1}{Q_0 x^{-a} + x^{0.2}}. \quad (23)$$

To reduce the number of retrieved parameters, I subsume the variables  $Q_1$  and  $\rho_d$  into  $q_c$  to create an effective mass mixing ratio,  $q_c^{\text{eff}}$

$$q_c^{\text{eff}} = \frac{Q_1}{\rho_d} q_c. \quad (24)$$

For typical silicate materials  $Q_1 \sim \rho_d$  ([Kitzmann & Heng 2018](#)), and so I expect the subsumed scaling to only be a small factor in the range  $\sim 1$ -10. Alternatively, representative constant values for  $Q_1$  and  $\rho_d$  for specific materials can be chosen (e.g. see [Kitzmann & Heng 2018](#)). This leaves the retrieved parameters to be:  $r_{\text{eff}}$ ,  $a$ ,  $Q_0$  and  $q_c^{\text{eff}}$ , the same number as the original [Fisher & Heng \(2018\)](#) scheme. This scheme can be easily extended to polydisperse size distributions, such as the

log-normal distribution. However, this is not used in the current study.

To reproduce a wavelength-independent grey cloud, the geometric optics limit ( $x \gg 1$ )  $Q_{\text{ext}} = 2$  can be assumed, which reduces the number of parameters to only  $r_{\text{eff}}$  and  $q_c$ . This allows a simple way to recover representative radii and mass mixing ratios without assuming any wavelength dependence on the cloud opacity, though practitioners wanting to further reduce the number of sampled parameters may wish to retain a single grey cloud opacity formulation.

For retrieving cloudy versus cloud-free atmosphere fractions, I use the simple linear combination of spectra with and without the effects of cloud opacity, for transmission and emission spectra, following [Line & Parmentier \(2016\)](#)

$$\Phi = \Phi_{\text{clid}} f_{\text{clid}} + (1 - f_{\text{clid}}) \Phi_{\text{cf}}, \quad (25)$$

where  $f_{\text{clid}}$  [0, 1] is the fraction of the spectra that contains cloud opacity,  $\Phi_{\text{clid}}$  the spectra including cloud opacity and  $\Phi_{\text{cf}}$  the cloud free spectra without the effects of cloud opacity.

### 2.5.3. Direct $n, k$ retrieval

I propose a new aerosol opacity parametrisation with the ability to quickly estimate the real ( $n$ ) and imaginary ( $k$ ) optical constants of the cloud particles directly. This allows the retrieval calculation to remain agnostic to the composition of the cloud particles, and compare the wavelength dependent structure of the retrieved optical constants to available databases.

In a retrieval context, I propose combining known analytic solutions to Mie theory to determine  $Q_{\text{ext}}$  wavelength dependently. I split the calculation into two size parameter regime approximations, Rayleigh for  $x \leq 1$  and Modified Anomalous Diffraction Theory (MADT) for  $x \geq 3$ . In the Rayleigh regime, the extinction efficiency is the sum of the scattering ( $Q_{\text{sca}}$ ) and absorption ( $Q_{\text{abs}}$ ) efficiencies given by ([Bohren & Huffman 1983](#))

$$Q_{\text{sca}} = \frac{8}{3} x^4 \Re \left[ \left( \frac{m^2 - 1}{m^2 + 2} \right)^2 \right], \quad (26)$$

and

$$Q_{\text{abs}} = 4x \Im \left[ \left( \frac{m^2 - 1}{m^2 + 2} \right) \left( 1 + \frac{x^2}{15} \left( \frac{m^2 - 1}{m^2 + 2} \right) \frac{m^4 + 27m^2 + 38}{2m^2 + 3} \right) \right], \quad (27)$$

where  $m = n + ik$ . For MADT, I follow the scheme described in [Moosmüller & Sorensen \(2018\)](#) with

$$Q_{\text{ext,MADT}} = (1 + 0.5C_2) Q_{\text{ext,ADT}} + Q_{\text{edge}}, \quad (28)$$

and

$$Q_{\text{abs,MADT}} = (1 + C_1 + C_2) Q_{\text{abs,ADT}}, \quad (29)$$

where  $C_1$ ,  $C_2$  and  $Q_{\text{edge}}$  are given in [Moosmüller & Sorensen \(2018\)](#) and  $Q_{\text{ADT}}$  are the values derived from Anomalous Diffraction Theory (ADT).

A problem with this approach is the inaccuracy of both Rayleigh and MADT in the intermediate size parameter regime  $1 \leq x \leq 10$ , though MADT is a significant improvement over ADT in this regime ([Moosmüller & Sorensen 2018](#)). To tackle this, I use a scaled smootherstep function to interpolate between the Rayleigh and MADT results between the range  $1 < x < 3$ , where the [0,1] smootherstep function is given by

$$S_2(x) = 6x^5 - 15x^4 + 10x^3, \quad (30)$$

which is re-scaled between 1 and 3.

Retrieving the individual  $n$  and  $k$  for each band is computationally infeasible, increasing the number of parameters to 100-1000s and likely to be highly degenerate and uninformative. I therefore use a parametrised, functional approach to reduce the number of parameters in the retrieval model, recovering the broad trends in  $n$  and  $k$ . For the  $n$  and  $k$  constants, I retrieve 12 spline nodes across the wavelength range of interest. These spline nodes are then used with a shape-preserving Piecewise Cubic Hermite Interpolation Polynomial (PCHIP) scheme to interpolate the  $n$  and  $k$  values across the wavelength range. Careful placement in wavelength is required for these nodes, with one required at both extremities of the wavelength range of interest. Placement can be more targeted through performing a cloud free retrieval first, then considering wavelength regions where suspected cloud absorption features may be present. For example, in the WASP-17b test case (Section 6.3), I aim to try recover the MIRI silicate absorption feature, and so concentrate the nodes around 7-12  $\mu\text{m}$ . I avoid placing nodes at the exact wavelengths of the observed data to discourage overfitting, instead placing them at regular intervals across the wavelength range and allowing the smooth interpolation scheme to provide the structure of the  $(n, k)$  coefficients. Overall, despite being an analytical approach, I find this method adds significant extra computational work during retrieval, slowing down convergence compared to the simpler fitting function from Kitzmann & Heng (2018) and Fisher & Heng (2018).

### 3. GAS PHASE OPACITIES

*Exo Skryer* has the ability to either use direct, ‘opacity sampled’ (OS) cross-section data or assume correlated-k (ck) with k-tables. I have included the functionality to read in the data formats used by the *TauREx 3* (Al-Refaie et al. 2021) and *petitRADTRANS* (Mollière et al. 2019) retrieval models available on the ExoMol<sup>1</sup> website (Chubb et al. 2021). In addition, I provide Python scripts to create custom OS or ck tables from the DACE<sup>2</sup> database. To mix individual species k-tables, I use the random overlap with resampling and rebinning (RORR) method (e.g. Amundsen et al. 2017) or, for transmission spectra, assuming random overlap through multiplication of the transmission functions of each species (e.g. Amundsen et al. 2017).

In this study, I mostly use a set of custom OS tables created using the *HELIOS-k* opacity calculator (Grimm & Heng 2015) at a constant spectral resolution of  $R = 20,000$  between 0.3  $\mu\text{m}$  and 30  $\mu\text{m}$ , with a temperature range of 50-6100 K and pressure range of  $10^{-8}$ -1000 bar. I include opacity data of H<sub>2</sub>O (Polyansky et al. 2018), CO<sub>2</sub> (Yurchenko et al. 2020), CO (Li et al. 2015), CH<sub>4</sub> (Yurchenko et al. 2024), NH<sub>3</sub> (Coles, Yurchenko & Tennyson 2019), H<sub>2</sub>S (Azzam et al. 2016), SO<sub>2</sub> (Underwood et al. 2016), Na (Kurucz & Bell 1995) and K (Kurucz & Bell 1995) where the citation associated with each molecule is the line-list reference used in *HELIOS-k* to produce the high-resolution ( $\Delta\nu = 0.01 \text{ cm}^{-1}$ ) original cross-section tabulated data.

#### 3.1. Free chemistry VMR retrieval

*Exo Skryer* is currently only able to perform ‘free’ retrievals assuming a constant vertical volume mixing ratio (VMR) of gas phase opacity sources, as well as implicitly assuming an

H<sub>2</sub> and He dominated atmospheric composition. I follow the scheme of Welbanks & Madhusudhan (2021) where the remainder of the gas VMR is composed of H<sub>2</sub> and He background gas, ensuring that  $\sum_i X_i = 1$ , given by

$$X_{\text{H}_2} = \frac{1 - \sum_{i, i \neq \text{He}, \text{H}_2}^n X_i}{1 + \frac{X_{\text{He}}}{X_{\text{H}_2}}}, \quad X_{\text{He}} = X_{\text{H}_2} \frac{X_{\text{He}}}{X_{\text{H}_2}}, \quad (31)$$

where the He to H<sub>2</sub> ratio is calculated from Asplund, Amarsi & Grevesse (2021)

$$\frac{X_{\text{He}}}{X_{\text{H}_2}} = 0.164. \quad (32)$$

As an option, useful for ultra hot Jupiters, but not used in the current study, I extend the formalism to include the H/H<sub>2</sub> to recover the effects of potential H<sub>2</sub> dissociation. I first define a H/H<sub>2</sub> VMR ratio as a retrievable quantity

$$f = \frac{X_{\text{H}}}{X_{\text{H}_2}}, \quad (33)$$

the remainder background fraction

$$X_{\text{bg}} = 1 - \sum_{i, i \neq \text{He}, \text{H}_2, \text{H}}^n X_i, \quad (34)$$

and He to H solar ratio

$$\epsilon_{\text{He}} = \frac{\text{He}}{\text{H}} = 0.082, \quad (35)$$

taken from Asplund, Amarsi & Grevesse (2021). I then define  $N_{\text{H}}$  to be a dimensionless abundance of hydrogen nuclei in the filling mixture

$$N_{\text{H}} = \frac{X_{\text{bg}}}{\frac{1+f}{2+f} + \epsilon_{\text{He}}}. \quad (36)$$

The H<sub>2</sub>, H and He VMRs are then

$$X_{\text{H}_2} = \frac{N_{\text{H}}}{f+2}, \quad X_{\text{H}} = f X_{\text{H}_2}, \quad X_{\text{He}} = \epsilon_{\text{He}} N_{\text{H}}. \quad (37)$$

I note that in certain circumstances  $X_{\text{H}} > X_{\text{H}_2}$ , which can be taken into account when setting prior bounds for the H/H<sub>2</sub> ratio. Combined with a simple electron number density fraction,  $f_{e^-}$ , retrieved parameter

$$f_{e^-} = \frac{n_{e^-}}{n_{\text{tot}}}, \quad (38)$$

where  $n_{e^-}$  [ $\text{cm}^{-3}$ ] is the electron number density and  $n_{\text{tot}}$  [ $\text{cm}^{-3}$ ] the background gas number density, this scheme enables a consistent way to recover free-free H<sup>-</sup> opacity, which can be an important continuum opacity source for ultra hot Jupiter atmospheres (e.g. Parmentier et al. 2018).

### 4. 1D TRANSMISSION SPECTRA

For the transmission spectra calculations, I use the 1D geometric, absorption only limit of the path distribution method presented in MacDonald & Lewis (2022) (Equation 19), which is based on the original Monte-Carlo formulation in Robinson (2017). This scheme enables a simple, fast method for calculating the transit limb, or slant, path. Briefly, this

<sup>1</sup> <https://www.exomol.com/>

<sup>2</sup> <https://dace.unige.ch/opacityDatabase/>

method constructs a geometric, slant path matrix,  $\mathcal{P}_{1D}$ , following

$$\mathcal{P}_{1D,il} = \begin{cases} 0, & r_{up,l} \leq b_i, \\ \frac{2}{\Delta r_l} \left( \sqrt{r_{up,l}^2 - b_i^2} \right), & r_{low,l} < b_i < r_{up,l}, \\ \frac{2}{\Delta r_l} \left( \sqrt{r_{up,l}^2 - b_i^2} - \sqrt{r_{low,l}^2 - b_i^2} \right), & r_{low,l} \geq b_i, \end{cases} \quad (39)$$

where  $r_l$  is the radius at layer  $l$  with upper  $r_{up,l}$  and lower  $r_{low,l}$  level interfaces, and  $b_i$  the impact parameter at layer  $i$ . The transit limb optical depth can then be related to the vertical optical depth through matrix multiplication

$$\tau_{trans} = \mathcal{P}_{1D} \cdot \Delta \tau_{vert}, \quad (40)$$

which can then be used in the transmission spectra equation (e.g. [Dobbs-Dixon & Agol 2013](#)). The utility of this approach comes from the fact that  $\mathcal{P}_{1D}$  is only required to be calculated once, and can be reused to find the slant optical path of any opacity component. Generalisation of the path matrix to multiple dimensions is derived in [MacDonald & Lewis \(2022\)](#).

## 5. 1D EMISSION SPECTRA

For the emission spectra calculations, I use the 1D, linear-in-tau,  $\delta$ -M scaled, extended absorption approximation scheme ( $\delta$ -EAA) described in [Lee \(2024\)](#), taking the 8-stream Gauss–Jacobi angles and weights in [Hogan \(2024\)](#) for the intensity to flux integration. In [Lee \(2024\)](#), this method was found to produce comparable top of atmosphere fluxes to within 2% of the Toon89 ([Toon et al. 1989](#)) and *DISORT* ([Stamnes et al. 1988](#)) methods in cloudy hot Jupiter scenarios.

For the brown dwarf retrievals, I follow the approach of [Kitzmann et al. \(2020\)](#), where the radius of the brown dwarf,  $R_{bd}$ , is set to a constant  $R_{jup}$  during retrieval, but includes a retrieved flux scaling parameter,  $f$ , through

$$F_{bd} = F_{toa} \left( \frac{R_{bd}}{D} \right)^2 = F_{toa} f \left( \frac{R_{jup}}{D} \right)^2, \quad (41)$$

where  $F_{toa}$  [ $\text{erg s}^{-1} \text{cm}^{-2} \text{cm}^{-1}$ ] is the wavelength dependent outgoing flux at the top of the atmosphere.  $f$  subsumes unknowns in the exact brown dwarf radius, the error in the distance measurements and potential scaling from any, assumed wavelength independent, atmospheric process, such as spatial inhomogeneity. The effective retrieved radius of the brown dwarf can be recovered as  $R_{bd} \approx \sqrt{f}$ .

## 6. RETRIEVAL MODEL EXAMPLES

In this section, I apply *Exo Skryer* across a variety of contemporary retrieval scenarios already published in the literature, or typical scenarios encountered by practitioners in the field. This allows a benchmark of the *Exo Skryer* framework to check that it is producing consistent results to other models. In addition, I publish the start-to-end completion time of each model. For brevity, I primarily focus on parameter estimation and not Bayesian evidence or model comparison for each scenario.

### 6.1. Transmission - HD 209458b

In an initial test of the *Exo Skryer* retrieval framework, I follow a HD 209458b transmission spectrum retrieval setup presented in [Barstow \(2020\)](#). [Barstow \(2020\)](#) used HST+Spitzer

TABLE 2  
HD 209458b PRE-JWST TRANSMISSION SPECTRUM RETRIEVAL SETUP AND RESULTS.

Parameter	Prior	Posterior
$R_\star [R_\odot]$	$\delta(1.187)$	-
$p_{bot}$ [bar]	$\delta(10)$	-
$p_{top}$ [bar]	$\delta(10^{-8})$	-
$p_{ref}$ [bar]	$\delta(10)$	-
$\rho_d$ [ $\text{g cm}^{-3}$ ]	$\delta(1)$	-
$Q_1$ [-]	$\delta(1)$	-
$\log_{10} g_{ref}$ [ $\text{cm s}^{-2}$ ]	$\mathcal{U}(2.7, 3.3)$	$3.21^{+0.05}_{-0.11}$
$R_{p,ref}$ [ $R_{jup}$ ]	$\mathcal{U}(1.1, 1.5)$	$1.37^{+0.01}_{-0.02}$
$T_{strat}$ [K]	$\mathcal{U}(100, 3000)$	$1181^{+153}_{-140}$
$\log_{10} \text{H}_2\text{O}$ [-]	$\mathcal{U}(-12, -2)$	$-5.06^{+0.17}_{-0.15}$
$\log_{10} \text{Na}$ [-]	$\mathcal{U}(-12, -2)$	$-6.64^{+0.27}_{-0.29}$
$\log_{10} \text{K}$ [-]	$\mathcal{U}(-12, -2)$	$-7.93^{+0.32}_{-0.27}$
$\log_{10} q_c$ [ $\text{g g}^{-1}$ ]	$\mathcal{U}(-12, 0)$	$-3.65^{+2.42}_{-3.61}$
$\log_{10} r_{cld}$ [ $\mu\text{m}$ ]	$\mathcal{U}(-3, 2)$	$-1.86^{+1.62}_{-1.08}$
$Q_0$ [-]	$\mathcal{U}(0.1, 65)$	$30.6^{+13.3}_{-16.6}$
$a_{cld}$ [-]	$\mathcal{U}(3, 7)$	$4.86^{+1.55}_{-1.37}$
$f_{cld}$ [-]	$\mathcal{U}(0, 1)$	$0.22^{+0.31}_{-0.15}$

data from [Sing et al. \(2016\)](#), retrieving  $\text{H}_2\text{O}$ , Na, K mixing ratios, as well as cloud parameters. I use a similar setup as [Barstow \(2020\)](#), namely, retrieving the same molecular species and using the stratosphere + adiabatic T-p parametrisation in [Barstow \(2020\)](#). I use the modified [Fisher & Heng \(2018\)](#) cloud opacity scheme (Section 2.5.2) with a constant condensed mass mixing ratio vertical profile, which in aggregate is highly similar to [Barstow \(2020\)](#). Using *dynesty* with 11 sampled parameters (Table 2), the elapsed time from start to finish of the retrieval model (OS at  $R = 20,000$ ) was 1 hour 6 minutes.

In Figure 3, I present the posterior distribution of the retrieval and best-fit median spectra. In comparing the posterior results to the retrievals performed with *NEMESIS* in [Barstow \(2020\)](#) (Figure 9), *Exo Skryer* is producing highly consistent results with respect to the  $\text{H}_2\text{O}$  mixing ratio, temperatures and reference radius. However, the main cloud opacity driver parameter,  $k_0$  in [Barstow \(2020\)](#) and  $q_c$  here remain quite unconstrained, with several orders of magnitude between the median and  $1\sigma$  confidence intervals, with bimodal structures present across the cloud parameters. This bimodal structure suggests that a large fraction of cloud mass contained in small,  $\sim 0.01 \mu\text{m}$  sized particles or a smaller mass mixing ratio with large  $\sim 1 \mu\text{m}$  particles can reasonably fit the data.  $Q_0$  and the scattering index,  $a_{cld}$ , are consistent with [Barstow \(2020\)](#), but *Exo Skryer* fits a smaller particle size and cloud fraction median pairing ( $r_{cld} = 0.135 \mu\text{m}$ ,  $f_{cld} = 0.22$ ) than [Barstow \(2020\)](#) ( $r_{eff} = 3.39 \mu\text{m}$ ,  $f_{cld} = 0.33$ ), though *Exo Skryer* has larger  $1\sigma$  ranges than those in [Barstow \(2020\)](#). Overall, the physical interpretation conclusions from this retrieval effort are highly similar to [Barstow \(2020\)](#), in that  $\text{H}_2\text{O}$  can be reasonably constrained to within  $\approx 0.1$  dex, but cloud structure information remains highly uncertain within the pre-JWST data.

### 6.2. Transmission - WASP-107b

WASP-107b ([Anderson et al. 2017](#)) is a warm-Neptune exoplanet, recently characterised by HST ([Kreidberg et al. 2018](#); [Spake et al. 2018](#)) and JWST ([Sing et al. 2024](#); [Welbanks et al. 2024](#); [Dyrek et al. 2024](#)). For the retrieval setup, I use the combined HST WFC3 + JWST NIRCcam + JWST MIRI data from [Welbanks et al. \(2024\)](#), and follow their free retrieval setup, as well as an offset for the MIRI data as in [Welbanks et al. \(2024\)](#). Using *dynesty* with 23 parameters (Table 3) the

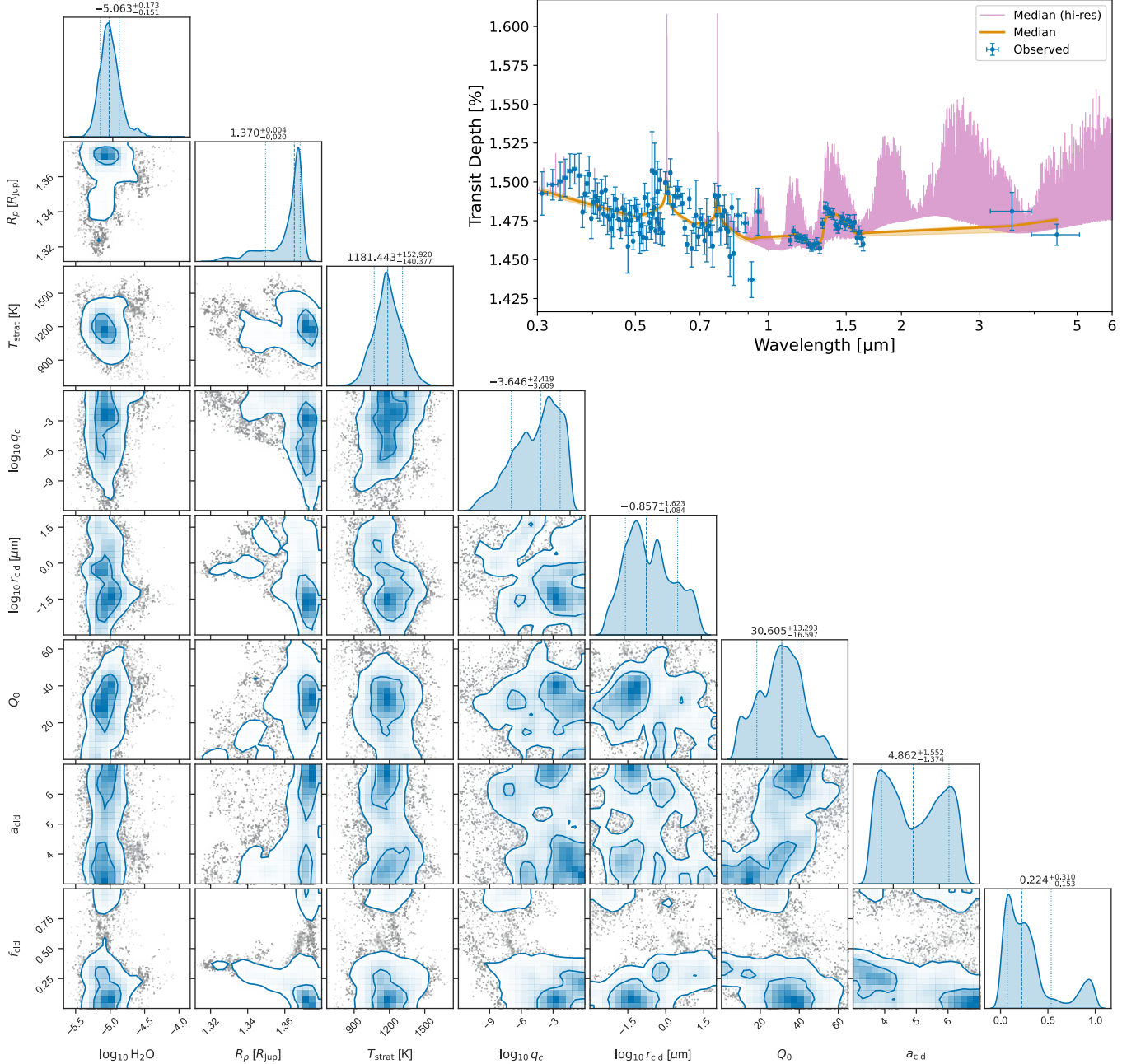


FIG. 3.— Equal weight posterior samples and kernel density estimation for the HD 209458b pre-JWST transmission spectra. The median and  $1\sigma$  confidence intervals are shown as the dashed and dotted lines respectively. The plot in the top right shows the best fit median spectra (orange) with  $1\sigma$  (shaded) region to the observed HD 209458b pre-JWST transmission spectra data (blue). The high-resolution median spectrum is in purple.

retrieval took 1 day 53 minutes (OS at  $R = 20,000$ ).

Figure 4 presents the posterior distribution and best-fit median spectra for the WASP-107b transmission spectra retrieval. I recover a very different free-retrieval outcome to that found in [Welbanks et al. \(2024\)](#), whereby I recover 1-2 dex lower VMR for all gas species. This is possibly a result of the assumed cloud structures and opacity, with [Welbanks et al. \(2024\)](#) using a grey deck and powerlaw approach, while here I use a non-grey, vertically varying mass mixing ratio scheme. The wavelength dependent approach used here allows the strong muting of the  $\text{H}_2\text{O}$  features at HST WFC3 wavelengths, but has a reduced cloud opacity at the longer wavelengths, enabling a smaller mixing ratio to recover the

required amplitude of the absorption features. I repeated the retrieval without the HST observational points to test the sensitivity of the cloud opacity to these points, but found little difference in the retrieval outcome. In contrast to the enhanced metallicity scenario recovered by [Welbanks et al. \(2024\)](#), the results suggest a thick, upper atmosphere cloud component which only allows the strongest lines to be probed in transmission, recovering a depleted atmosphere, driven by the missing information content provided by spectral windows for each species. The post-processed transmission spectra is reminiscent of studies that performed high-resolution modelling with strong upper atmosphere cloud opacity (e.g. [Gandhi, Brogi & Webb 2020](#)).

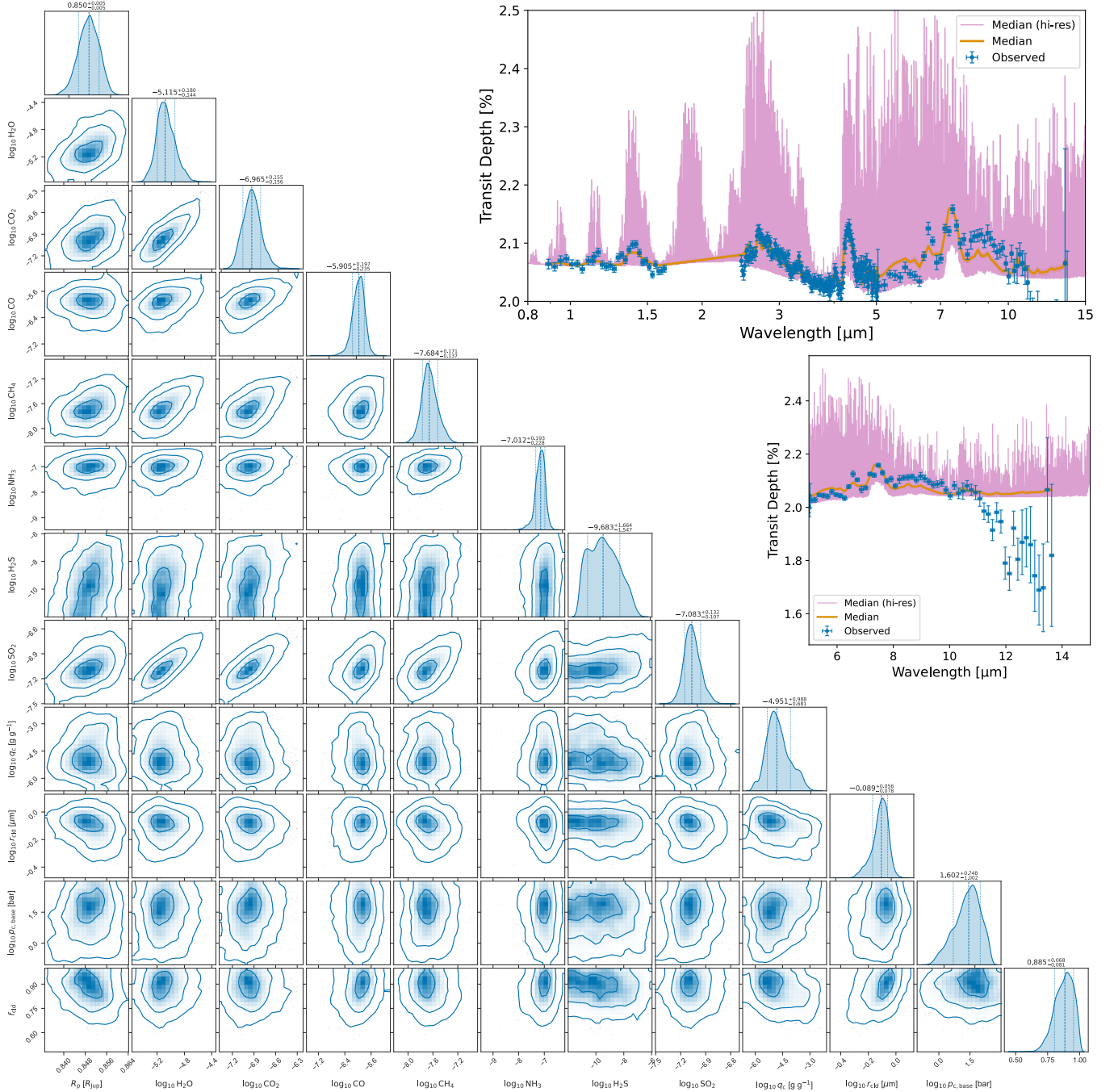


Fig. 4. — Equal weight posterior samples and kernel density estimation for the WASP-107b JWST transmission spectra. The median and  $1\sigma$  confidence intervals are shown as the dashed and dotted lines respectively. The top left plots show the observational data (blue points), median model with  $1\sigma$  ranges (orange) and high-resolution median model (purple).

I perform an additional retrieval without including the MIRI data from Welbanks et al. (2024), which tests the sensitivity of the species VMR results to the MIRI. The posterior corner plot for this retrieval is shown in Appendix A. In this case, I reproduce well the enhanced metallicity retrieved VMRs from Welbanks et al. (2024), in contrast to the reduced metallicity recovered including the MIRI data. This suggests that the MIRI data significantly influences the result of the retrieval efforts, however, it is unclear exactly why this is the case. Possibly, the additional MIRI cloud feature fitting included in the Welbanks et al. (2024) free retrievals reduced the overall

sensitivity of the MIRI data on the gas phase VMRs.

Overall, despite the differences found in the initial modelling, I see no particular failing on the part of *Exo Skryer*, in that the retrieval results look reasonable and plausible. The results of Sing et al. (2024), Welbanks et al. (2024) and those presented here warrant further JWST observations of this planet to better constrain the cloud coverage, in particular to fill the wavelength gap between HST WFC3 and JWST NIRCcam.

### 6.3. Transmission - WASP-17b

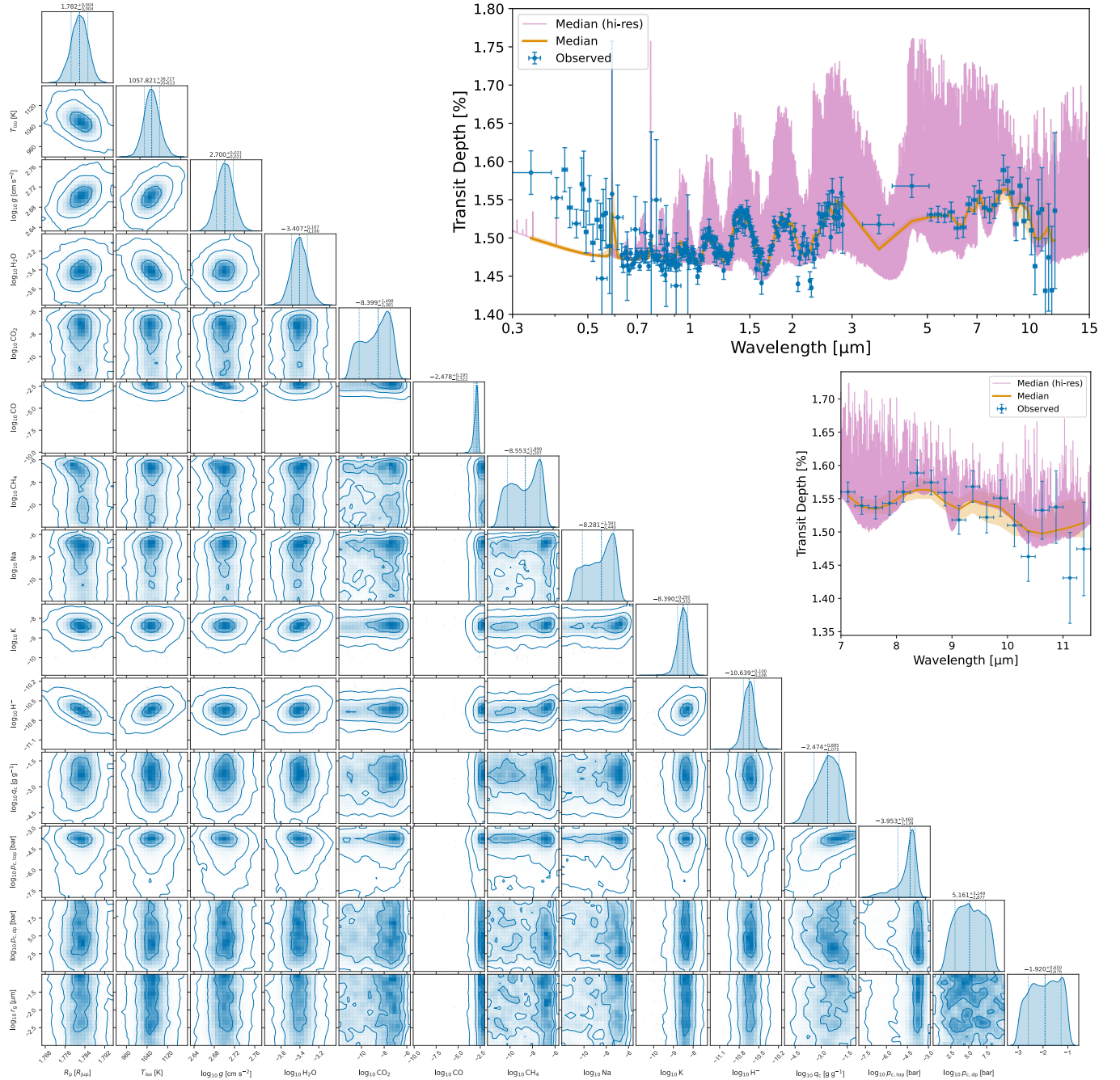


Fig. 5.— Equal weight posterior samples and kernel density estimation for the WASP-17b HST and JWST combined transmission spectra retrieval from Louie et al. (2025). The median and  $1\sigma$  confidence intervals are shown as the dashed and dotted lines respectively. The plots in the top right show the best fit median spectra (orange) with  $1\sigma$  (shaded) region to the observed transmission spectra data (blue), taken from Louie et al. (2025), for the full spectral range (top right) and MIRI LRS wavelength range (middle right). The high-resolution median spectrum is in purple.

To test the proposed direct optical constant retrieval scheme, I perform a similar retrieval setup to that performed for WASP-17b in Louie et al. (2025), who published new SOSS data and combined them with the previous HST STIS+WFC3 (Alderson et al. 2022) and MIRI LRS (Grant et al. 2023) data. I follow the enhanced ‘B’ scheme from Louie et al. (2025), which included retrieval of  $\text{H}_2\text{O}$ ,  $\text{CO}$ ,  $\text{CO}_2$ ,  $\text{CH}_4$ ,  $\text{Na}$ ,  $\text{K}$  and  $\text{H}^-$  (bound-free). I follow similar priors and setup as the *POSEIDON* (MacDonald 2023) framework used in Louie et al. (2025), assuming an isothermal 100 layer atmosphere evenly log-spaced between 100 and  $10^{-8}$  bar. I in-

clude Rayleigh scattering from  $\text{H}_2$  and  $\text{He}$  as well as CIA from  $\text{H}_2$ - $\text{H}_2$  and  $\text{H}_2$ - $\text{He}$  pairs. For the cloud model, I use the same slab profile approach used in *POSEIDON*, but only retrieve the cloud properties in the 7-11.5  $\mu\text{m}$  wavelength range in order to focus on retrieving the  $n$  and  $k$  constants for the cloud absorption features. The spectrum is therefore cloud free outside this wavelength range. I take the HST + SOSS + Spitzer + MIRI spectrum presented in Louie et al. (2025), adding an offset to the MIRI data as retrieved in Louie et al. (2025). I perform two OS retrievals, one at  $R = 10,000$  and one at  $R = 20,000$ . Using *dynesty* with 40 sampled parameters (Table 4),

TABLE 3  
WASP-107b JWST TRANSMISSION SPECTRUM RETRIEVAL SETUP AND RESULTS.

Parameter	Prior	Posterior
$R_\star [R_\odot]$	$\delta(0.67)$	-
$p_{\text{bot}}$ [bar]	$\delta(1000)$	-
$p_{\text{top}}$ [bar]	$\delta(10^{-8})$	-
$p_{\text{ref}}$ [bar]	$\delta(10)$	-
$\rho_d$ [g cm $^{-3}$ ]	$\delta(1.0)$	-
$Q_1$ [-]	$\delta(1.0)$	-
$\log_{10} g$ [cm s $^{-2}$ ]	$\mathcal{U}(2.0, 3.5)$	$2.69^{+0.03}_{-0.01}$
$R_{p,\text{ref}}$ [ $R_{\text{jup}}$ ]	$\mathcal{U}(0.66, 1.22)$	$0.85^{+0.01}_{-0.01}$
$T_0$ [K]	$\mathcal{U}(100, 4000)$	$859^{+92}_{-80}$
$\log_{10} p_0$ [bar]	$\mathcal{U}(-7, -4)$	$-6.1^{+0.9}_{-0.6}$
$\log_{10} p_1$ [bar]	$\mathcal{U}(-4, -1)$	$-1.9^{+0.5}_{-0.6}$
$\log_{10} p_2$ [bar]	$\mathcal{U}(-1, 3)$	$1.2^{+1.2}_{-1.3}$
$\alpha_1$ [K $^{-1/2}$ ]	$\mathcal{U}(0.02, 2)$	$0.99^{+0.36}_{-0.32}$
$\alpha_2$ [K $^{-1/2}$ ]	$\mathcal{U}(0.02, 2)$	$0.78^{+0.18}_{-0.14}$
$\log_{10} \text{H}_2\text{O}$ [-]	$\mathcal{U}(-12, -2)$	$-5.12^{+0.18}_{-0.14}$
$\log_{10} \text{CO}_2$ [-]	$\mathcal{U}(-12, -2)$	$-6.97^{+0.16}_{-0.16}$
$\log_{10} \text{CO}$ [-]	$\mathcal{U}(-12, -2)$	$-5.91^{+0.20}_{-0.24}$
$\log_{10} \text{CH}_4$ [-]	$\mathcal{U}(-12, -2)$	$-7.68^{+0.17}_{-0.14}$
$\log_{10} \text{NH}_3$ [-]	$\mathcal{U}(-12, -2)$	$-7.01^{+0.19}_{-0.23}$
$\log_{10} \text{H}_2\text{S}$ [-]	$\mathcal{U}(-12, -2)$	$-9.68^{+1.67}_{-1.55}$
$\log_{10} \text{SO}_2$ [-]	$\mathcal{U}(-12, -2)$	$-7.08^{+0.13}_{-0.11}$
$\log_{10} r_{\text{cld}}$ [ $\mu\text{m}$ ]	$\mathcal{U}(-3, 2)$	$-0.09^{+0.06}_{-0.06}$
$\log_{10} q_{\text{c,base}}$ [g g $^{-1}$ ]	$\mathcal{U}(-12, 0)$	$-4.95^{+0.98}_{-0.68}$
$\log_{10} p_{\text{c,base}}$ [bar]	$\mathcal{U}(-8, 3)$	$1.60^{+0.75}_{-1.00}$
$\log_{10} \alpha_{\text{cld}}$ [-]	$\mathcal{U}(-2, 2)$	$-0.23^{+0.18}_{-0.21}$
$Q_0$ [-]	$\mathcal{U}(1, 65)$	$39.1^{+16.1}_{-20.1}$
$a_{\text{cld}}$ [-]	$\mathcal{U}(2, 5)$	$4.45^{+0.41}_{-0.60}$
$f_{\text{cld}}$ [-]	$\mathcal{U}(0, 1)$	$0.89^{+0.07}_{-0.08}$
$\Delta_{\text{MIRI}}$ [ppm]	$\mathcal{U}(-50, 500)$	$195.8^{+37.8}_{-31.8}$

TABLE 4  
WASP-17b JWST TRANSMISSION SPECTRUM RETRIEVAL SETUP AND RESULTS.

Parameter	Prior	Posterior
$R_\star [R_\odot]$	$\delta(1.583)$	-
$p_{\text{bot}}$ [bar]	$\delta(100)$	-
$p_{\text{top}}$ [bar]	$\delta(10^{-8})$	-
$p_{\text{ref}}$ [bar]	$\delta(10)$	-
$\rho_d$ [g cm $^{-3}$ ]	$\delta(2.5)$	-
$\log_{10} g$ [cm s $^{-2}$ ]	$\mathcal{U}(2.2, 3.0)$	$2.7^{+0.02}_{-0.02}$
$R_{p,\text{ref}}$ [ $R_{\text{jup}}$ ]	$\mathcal{U}(1.5895, 2.1505)$	$1.78^{+0.01}_{-0.01}$
$T_{\text{iso}}$ [K]	$\mathcal{U}(400, 2300)$	$1057^{+39}_{-36}$
$\log_{10} \text{H}_2\text{O}$ [-]	$\mathcal{U}(-12, -2)$	$-3.41^{+0.11}_{-0.10}$
$\log_{10} \text{CO}_2$ [-]	$\mathcal{U}(-12, -2)$	$-8.45^{+1.50}_{-2.38}$
$\log_{10} \text{CO}$ [-]	$\mathcal{U}(-12, -2)$	$-2.48^{+0.12}_{-0.32}$
$\log_{10} \text{CH}_4$ [-]	$\mathcal{U}(-12, -2)$	$-8.55^{+1.90}_{-2.28}$
$\log_{10} \text{Na}$ [-]	$\mathcal{U}(-12, -2)$	$-8.28^{+1.59}_{-2.44}$
$\log_{10} \text{K}$ [-]	$\mathcal{U}(-12, -2)$	$-8.39^{+0.31}_{-0.31}$
$\log_{10} \text{H}^-$ [-]	$\mathcal{U}(-12, -2)$	$-10.64^{+0.10}_{-0.11}$
$\log_{10} r_g$ [ $\mu\text{m}$ ]	$\mathcal{U}(-3, -1)$	$-1.92^{+0.65}_{-0.68}$
$\log_{10} q_c$ [g g $^{-1}$ ]	$\mathcal{U}(-12, 0)$	$-2.47^{+1.89}_{-1.10}$
$\log_{10} p_{\text{c,top}}$ [bar]	$\mathcal{U}(-8, 3)$	$-3.96^{+0.36}_{-1.14}$
$\log_{10} p_{\text{c,dp}}$ [bar]	$\mathcal{U}(0, 10)$	$5.16^{+3.15}_{-2.88}$
$n_{0\dots12}$ [-]	$\mathcal{U}(0.3, 4.0)$	Figure 6
$\log_{10} k_{0\dots12}$ [-]	$\mathcal{U}(-6, 1)$	Figure 6

the elapsed time from start to finish of the retrieval model was 13 hours 41 minutes for the  $R = 10,000$  model and 1 day 19 minutes for the  $R = 20,000$  model. I found both resolutions showed highly comparable posterior distributions, suggesting insensitivity to the spectral resolution in this scenario.

Figure 5 presents the posterior and best-fit median model compared to the observational data for the  $R = 20,000$  model. The retrieval produces similar results to Louie et al. (2025), with the main difference being a couple magnitudes larger CO retrieved here compared to Louie et al. (2025). This is probably driven by the lack of a cloud opacity continuum, requiring a larger CO opacity to compensate for the large Spitzer  $4.5\mu\text{m}$  observational point.

In addition, Figure 5 also contains a zoom in on the 7-12  $\mu\text{m}$  region, where the  $(n, k)$  optical constants were retrieved. Here, the absorption feature around  $8.7\mu\text{m}$  is well described by the retrieved parameters, and the absorption peak shifted slightly blueward compared to the  $\text{SiO}_2$  quartz retrieval models in Louie et al. (2025). A secondary peak is seen at around  $9.5\mu\text{m}$ , suggesting the presence of a secondary cloud absorption band component, though the  $1\sigma$  confidence region is wider in this wavelength regime. The retrieval results suggest a mass mixing ratio of  $q_c \sim 10^{-2.5}$ , which is in line with expectations of the Si abundance at around 10-100x Solar metallicity (Asplund, Amarsi & Grevesse 2021).

In Figure 6, I compare the retrieved optical constant the glassy  $\alpha\text{-SiO}_2$  quartz constants from Zeidler, Posch & Mutschke (2013) commonly used in the literature. Though large uncertainties remain, for the  $k$  constant, the model suggests a material highly consistent with  $\text{SiO}_2$ , but with a slightly broader, bluer bump. This conforms with the fitting of this feature to various  $\text{SiO}_2$  polymorphs in Moran, Marley & Crossley (2024), who found the absorption peak of the  $\text{SiO}_2$  can shift dependent on the crystalline state of the mineral. The scattering component of the opacity is not dominant in this wavelength range, which heavily limits the ability of the retrieval to produce constraints on the  $n$  constant. Overall, this discrepancy between the retrieved  $k$  and the database  $\text{SiO}_2$  warrants further detailed investigations into the material

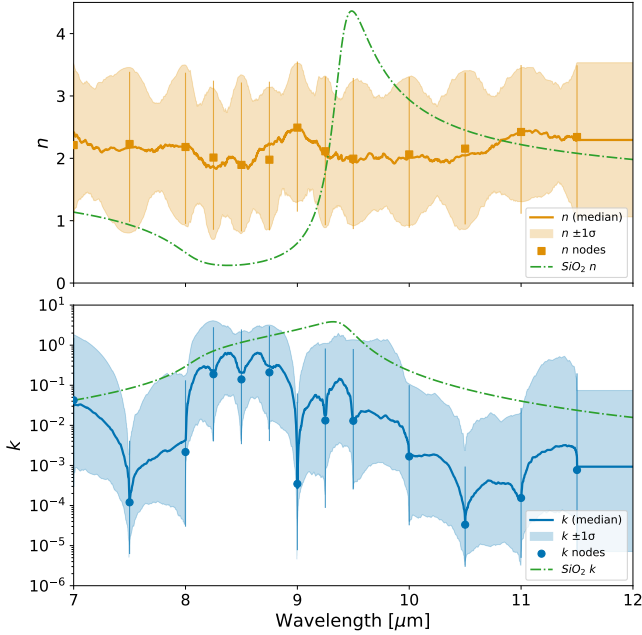


FIG. 6.— Direct  $n$  (top, orange) and  $k$  (bottom, blue) retrieval results from the WASP-17b transmission spectrum test. The glassy  $\alpha\text{-SiO}_2$  optical constants from Zeidler, Posch & Mutschke (2013) are plotted with the dash-dot green lines.

TABLE 5  
HD 189733b JWST EMISSION SPECTRUM RETRIEVAL SETUP AND RESULTS.

Parameter	Prior	Posterior
$R_\star [R_\odot]$	$\delta(0.765)$	-
$p_{\text{bot}}$ [bar]	$\delta(100)$	-
$p_{\text{top}}$ [bar]	$\delta(10^{-8})$	-
$p_{\text{ref}}$ [bar]	$\delta(10)$	-
$\rho_d$ [g cm $^{-3}$ ]	$\delta(2.5)$	-
$f_{\text{hem}}$ [-]	$\delta(0.25)$	-
$\log_{10} g$ [cm s $^{-2}$ ]	$\mathcal{U}(2.7, 3.3)$	$3.12^{+0.12}_{-0.14}$
$R_{p,\text{ref}}$ [ $R_{\text{jup}}$ ]	$\mathcal{U}(1.0, 1.2)$	$1.08^{+0.01}_{-0.01}$
$T_{\text{eq}}$ [K]	$\mathcal{U}(500, 2000)$	$1670^{+37}_{-44}$
$T_{\text{int}}$ [K]	$\mathcal{U}(100, 600)$	$332^{+156}_{-134}$
$\log_{10} \kappa_{\text{ir}}$ [cm $^2$ g $^{-1}$ ]	$\mathcal{U}(-6, 2)$	$-3.71^{+0.50}_{-0.68}$
$\log_{10} \gamma_v$ [-]	$\mathcal{U}(-3, 2)$	$-1.58^{+0.61}_{-0.48}$
$q_{\text{irr},0}$ [-]	$\mathcal{U}(0, 0.66)$	$0.16^{+0.06}_{-0.07}$
$\log_{10} p_t$ [bar]	$\mathcal{U}(-7, 1)$	$-1.95^{+0.25}_{-0.27}$
$\beta$ [-]	$\mathcal{U}(0.1, 1)$	$0.53^{+0.15}_{-0.13}$
$\log_{10} \text{H}_2\text{O}$ [-]	$\mathcal{U}(-12, -1)$	$-2.36^{+0.31}_{-0.30}$
$\log_{10} \text{CO}_2$ [-]	$\mathcal{U}(-12, -1)$	$-5.15^{+0.29}_{-0.26}$
$\log_{10} \text{CO}$ [-]	$\mathcal{U}(-12, -1)$	$-1.89^{+0.39}_{-0.40}$
$\log_{10} \text{CH}_4$ [-]	$\mathcal{U}(-12, -1)$	$-7.69^{+0.87}_{-0.79}$
$\log_{10} r_{\text{cid}}$ [ $\mu\text{m}$ ]	$\mathcal{U}(-3, 2)$	$0.97^{+0.17}_{-0.15}$
$\log_{10} q_{c,\text{base}}$ [g g $^{-1}$ ]	$\mathcal{U}(-12, 0)$	$-3.85^{+0.75}_{-0.43}$
$\log_{10} p_{c,\text{base}}$ [bar]	$\mathcal{U}(-6, 1)$	$-2.11^{+1.01}_{-0.87}$
$\log_{10} \alpha_c$ [-]	$\mathcal{U}(-2, 2)$	$-0.56^{+0.80}_{-0.74}$
$n_{0...12}$ [-]	$\mathcal{U}(0.3, 4.0)$	Figure 8
$\log_{10} k_{0...12}$ [-]	$\mathcal{U}(-6, 1)$	Figure 8

compositions of the cloud particles in the WASP-17b atmosphere.

#### 6.4. Emission - HD189733 b

In this test, I perform a dayside emission spectra retrieval test on the canonical hot Jupiter HD 189733b. I use a combined HST WFC3 (Changeat et al. 2022), JWST NIRCcam (Zhang et al. 2025) and JWST MIRI LRS (Inglis et al. 2024) dayside emission spectrum. I use the direct ( $n, k$ ) retrieval method in the MIRI wavelength regime, to try recover the optical constants of the suspected aerosol absorption feature seen in Inglis et al. (2024). Using *dynesty*, the retrieval had 43 sampled parameters (Table 5), with the elapsed time from start to finish being 1 day 12 hours 46 minutes (OS at  $R = 20,000$ ).

Figure 7 presents the posterior distribution and best fit median models compared to the observational data. I recover a generally metallicity enhanced atmosphere, with  $\text{H}_2\text{O}$ , CO and  $\text{CO}_2$  VMRs around 5-10 $\times$  Solar, in line with previous retrieval modelling (Zhang et al. 2025). Overall, the JWST NIRCcam and MIRI data are well fit by the median model, with the HST WFC3 less well fit. This suggests potential multi-dimensional effects may be present, such as a hotspot that would increase near-IR fluxes but not significantly influence redder wavelengths. Alternatively, a significant near-IR albedo from high altitude clouds would also raise the near-IR spectral flux (Evans et al. 2013). Multiple T-p profile techniques, hotspot emulation or dilution factors (e.g. Feng et al. 2016; Taylor et al. 2020; Schlawin et al. 2024; Wisser et al. 2025) may therefore be appropriate to apply to this planet, but this is outside the scope of this example study. However, a uniform data reduction between the HST and JWST data would need to be carried out to make a fair comparison.

Figure 8 shows the recovered ( $n, k$ ) optical constants from the retrieval model. Similar to the WASP-17b retrieval, I find that the  $n$  constant is unconstrained, with large uncertainty

TABLE 6  
GLIESE 229 B BROWN DWARF EMISSION SPECTRUM RETRIEVAL SETUP AND RESULTS.

Parameter	Prior	Posterior
$p_{\text{bot}}$ [bar]	$\delta(1000)$	-
$p_{\text{top}}$ [bar]	$\delta(10^{-4})$	-
$p_{\text{ref}}$ [bar]	$\delta(10)$	-
$D$ [pc]	$\delta(10)$	-
$R_{\text{bd}}$ [ $R_{\text{jup}}$ ]	$\mathcal{U}(0.3, 2.2)$	$0.94^{+0.04}_{-0.03}$
$M_{\text{bd}}$ [ $M_{\text{jup}}$ ]	$\mathcal{U}(1, 80)$	$77.9^{+1.6}_{-3.2}$
$T_{\text{int}}$ [K]	$\mathcal{U}(500, 1500)$	$1142^{+32}_{-27}$
$T_{\text{ratio}}$ [-]	$\mathcal{U}(0, 1)$	$0.48^{+0.03}_{-0.05}$
$\log_{10} \kappa_{\text{ir}}$ [cm $^2$ g $^{-1}$ ]	$\mathcal{U}(-4, 0)$	$-1.70^{+0.05}_{-0.06}$
$\log_{10} p_t$ [bar]	$\mathcal{U}(-2, 3)$	$0.86^{+0.08}_{-0.07}$
$\beta$ [-]	$\mathcal{U}(0, 1)$	$0.96^{+0.03}_{-0.06}$
$\log_{10} \text{H}_2\text{O}$ [-]	$\mathcal{U}(-12, -2)$	$-3.44^{+0.01}_{-0.01}$
$\log_{10} \text{CO}$ [-]	$\mathcal{U}(-12, -2)$	$-4.20^{+0.15}_{-0.16}$
$\log_{10} \text{CH}_4$ [-]	$\mathcal{U}(-12, -2)$	$-3.26^{+0.01}_{-0.01}$
$\log_{10} \text{NH}_3$ [-]	$\mathcal{U}(-12, -2)$	$-4.63^{+0.01}_{-0.03}$
$\log_{10} \text{Na}$ [-]	$\mathcal{U}(-12, -2)$	$-7.08^{+0.03}_{-0.22}$
$\log_{10} \text{K}$ [-]	$\mathcal{U}(-12, -2)$	$-6.90^{+0.02}_{-0.02}$

across the wavelength regime. However, for the  $k$  constant, two main features are present; one bluer than the  $\text{SiO}_2$  absorption peak (Zeidler, Posch & Mutschke 2013) data and a redder peak at  $\approx 10.5 \mu\text{m}$ . A possibility is that the bluer peak is caused by a  $\text{SiO}_2$  polymorph different to quartz as seen in the Moran, Marley & Crossley (2024) study, who investigated the WASP-17b MIRI cloud absorption feature. The redder peak is harder to compare to other species, but may be an amorphous silicate material, as those materials generally exhibit a redder peak compared to quartz (e.g. Wakeford & Sing 2015; Kitzmann & Heng 2018; Mullens, Lewis & MacDonald 2024). Overall, this suggests that the commonly assumed  $\alpha$ - $\text{SiO}_2$  quartz material may be a strong assumption for this exoplanet. I recover a median cloud base mass mixing ratio of  $q_{c,\text{base}} \approx 10^{-4}$ , which is in line with around a 5-10 $\times$  Solar enhancement of Si (Asplund, Amarsi & Grevesse 2021).

#### 6.5. Emission - Gliese 229 B

To exhibit the brown dwarf retrieval system in *Exo Skryer*, I perform a retrieval on the T-dwarf Gliese 229B, following the setup and collated observational data from Calamari et al. (2022). Calamari et al. (2022) used the *Brewster* brown dwarf retrieval code presented in Burningham et al. (2017). Despite Gliese 229B being recently confirmed to be a binary system (Brandt et al. 2021; Xuan et al. 2024a; Whitebook et al. 2024), the quality of the spectral data and numerous previous modelling efforts on this system provide a useful comparison benchmark. I perform a ‘free’ retrieval, allowing an unconstrained mass to be sampled, and assuming a cloud free atmosphere to compare directly to the same scenario presented in Calamari et al. (2022). Using *dynesty*, with 14 sampled parameters (Table 6), the retrieval took 5 hours 26 minutes (OS at  $R = 20,000$ ).

Comparing to the results of Calamari et al. (2022), I retrieve highly similar VMRs for all gas species as well as T-p profile, suggesting both retrieval outcomes are generally consistent with respect to the variables sensitive to radiative-transfer outcomes. The integrated spectrum of the median model resulted in  $T_{\text{eff}} = 915$  K, which is around 100 K hotter than that retrieved in Calamari et al. (2022). However, I retrieve a higher median mass at  $M_{\text{bd}} = 78 M_{\text{jup}}$ , compared to the 50-72  $M_{\text{jup}}$  range across the models performed in Calamari et al. (2022), with a consistent effective radius between

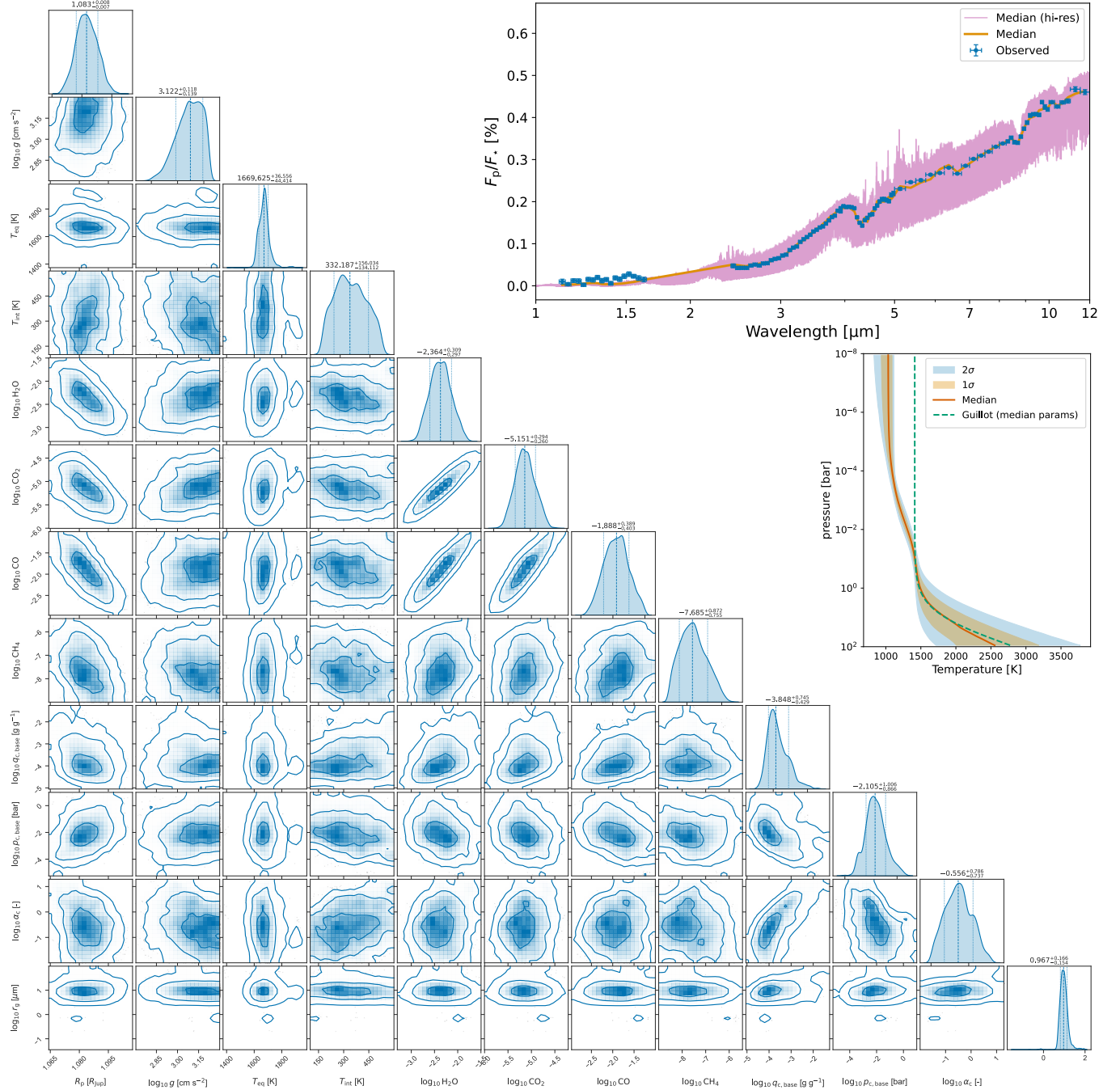


FIG. 7.— Equal weight posterior samples and kernel density estimation for the HD 189733b HST and JWST dayside emission spectra retrieval. The median and  $1\sigma$  confidence intervals are shown as the dashed and dotted lines respectively. The plots in the top right show the best fit median spectra (orange) with  $1\sigma$  (shaded) region to the observed transmission spectra data (blue), taken from [Changeat et al. \(2022\)](#); [Zhang et al. \(2025\)](#) and [Inglis et al. \(2024\)](#) for the full spectral range (top right). The high-resolution median spectrum is in purple. The middle right plot shows the retrieved modified Guillot T-p profile (Sect. 2.4.4), compared to the original formulation (green dashed line).

this study and [Calamari et al. \(2022\)](#). The retrieved mass is pushing against the upper prior range, showing *Exo Skryer* exhibits the well-known Gravity-Radius-Composition degeneracy present in brown dwarf fitting and retrieval modelling of spectra (e.g. [Burrows et al. 2001](#); [Zalesky et al. 2019](#); [Kitzmann et al. 2020](#); [Lueber et al. 2022](#)). The retrieval results are more consistent with the [Kawashima et al. \(2025\)](#) study, who use ground-based high-resolution spectral data from Subaru/IRD and applied the *ExoJAX* retrieval model ([Kawahara et al. 2022, 2025](#)). They retrieve a larger mass,

$\sim 100 M_{\text{Jup}}$ , in their free retrievals, and discuss the degeneracies encountered as applied to high-resolution spectra in detail. Utilising JWST MIRI ([Xuan et al. 2024b](#)) and future JWST NIRSpec (GO #3762 P.I. J. Xuan) data in conjunction with current data should provide much needed clarity on the combined and individual parameters of each brown dwarf.

## 7. DISCUSSION

Through the numerous test retrievals presented in this study, *Exo Skryer* has been shown to produce highly consistent and

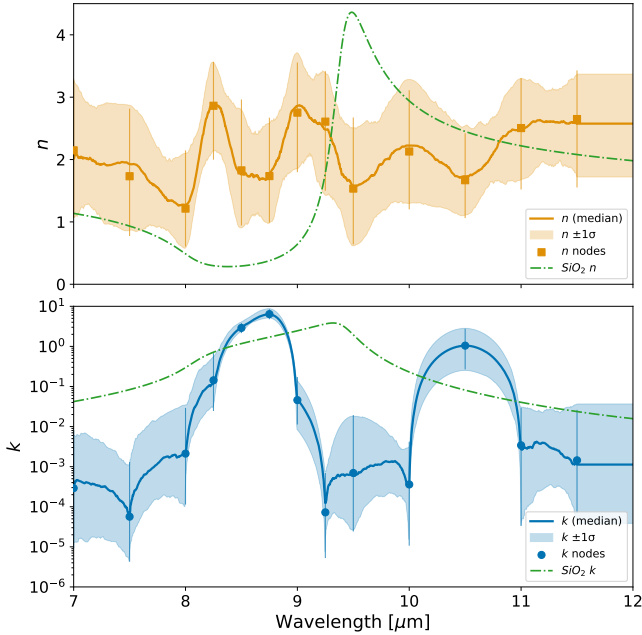


Fig. 8.— Direct  $n$  (top orange) and  $k$  (bottom blue) retrieval results from the HD 189733b emission spectrum test. The glassy  $\alpha$ -SiO<sub>2</sub> optical constants from Zeidler, Posch & Mutschke (2013) are plotted with the dash-dot green lines.

compatible retrieval outcomes to a wide variety of different frameworks, from *NEMESIS* (Irwin et al. 2008), *petitRADTRANS* (Mollière et al. 2019), *POSEIDON* (MacDonald 2023) and *Brewster* (Bunningham et al. 2017). Though *Exo Skryer* does not yet have all the features present in the above cited frameworks, in particular currently lacking a chemical equilibrium solver, I have developed several new methods for *Exo Skryer* that may be of use in other models, namely the modified Milne and Guillot T-p profiles, non-grey cloud opacity methodology, and direct  $n$  and  $k$  optical constant retrieval.

In Section 2.5.3, I proposed a new direct ( $n$ ,  $k$ ) optical constant retrieval method. I found that the recovered optical constants are generally consistent with the commonly assumed SiO<sub>2</sub> material composition, but the main peak is bluer for both the WASP-17b and HD 189733b data, suggesting that the optical constants for the  $\alpha$ -SiO<sub>2</sub> may not be representative of the real cloud materials inside these hot atmospheres. In addition, for the HD 189733b dayside emission case, I find evidence for a possible secondary absorption feature at around 10.5  $\mu$ m. Moran, Marley & Crossley (2024) collated or derived optical constants for several SiO<sub>2</sub> polymorphs, showing that the specific formation conditions of the material is important in setting the shapes and peaks of the optical constants. However, as noted in Moran, Marley & Crossley (2024) this data was patchy and possibly unreliable, warranting new laboratory experiments that produce exoplanet cloud samples at representative temperature conditions of these atmosphere that explore different crystalline states and potential mineral mixtures.

For both the WASP-17b and HD 189733b cases, I intentionally only targeted the observed absorption region between 7-12  $\mu$ m, ignoring the effects of cloud opacity on the rest of the spectrum. A more complete retrieval methodology may be developed in the future, able to both retrieve optical constants at specific wavelengths and utilise a more general cloud scheme across the wavelength range. In testing, I first attempted a Kramers–Kronig (KK) approach, retrieving the  $k$

constant and using KK to calculate the  $n$ , similar to Irwin et al. (2018). However, I found the computation to be too inefficient, and the retrieval unable to converge on a reasonable timescale. An alternative may be to post-process the retrieved  $k$  values using KK to produce physically consistent  $n$  values that can be compared to current databases. This is left to future iterations of the model.

In this study, I used an Nvidia GeForce RTX 4090 GPU for all retrievals which is sub-optimal for several reasons:

- Double precision, 64 bit operations, critical for accurate forward model operation, are not optimised in the 4090 consumer grade architecture compared to server-grade equipment, reducing the numerical operation speed significantly.
- The 4090 was released in 2022, and is considered last generation hardware. Newer GPUs may be even up to 10-100% faster.

Therefore, I expect the specific values quoted in this study can be improved upon, possibly 2-5 $\times$  using an optimised hardware setup.

The speed tests in Section 2.2.1 show that using *pymultinest* is around two times faster than *dynesty* for the 11 parameter HD 209459b case study. Should expediency at lower dimensionality be required, *pymultinest* offers the fastest retrieval option presented in this study. For significantly larger dimensionality ( $\sim 50+$ ), other frameworks have been shown to be more efficient and robust (e.g. Handley, Hobson & Lasenby 2015; Speagle 2020). Extremely parallel nested sampling frameworks such as *blackjax-ns* (Yallup, Kroupa & Handley 2025) are also being developed and have been applied to black hole merger events (Prathaban et al. 2025). This method fully parallelises over live-points as well as likelihood calculations. This is an active area of research, but shows promise to be the fastest sampler in the near future.

## 8. CONCLUSION

With worldwide high-performance computing infrastructure continuing to hybridise to include a substantial GPU complement, computational demanding scientific codes such as exoplanet and brown dwarf retrieval models are shifting towards making efficient use of this new infrastructure landscape. An added advantage of using highly-parallel models is that runtimes are significantly reduced compared to serial implementations, allowing faster exploration of Bayesian evidence and parameter estimation in the wide-wavelength, medium spectral resolution JWST era.

I present a new sub-stellar atmosphere retrieval model, *Exo Skryer*, that leverages the JAX library for Python. The design of *Exo Skryer* allows computation on CPU and GPU systems, as well as a mixture of the two, where in this study I found that the hybrid CPU+GPU option to be optimal, enabling robust, well tested sampling frameworks to be used while heavily accelerating forward model evaluations. This significantly reduces the time for retrieval completion, down to minutes for simple models and handfuls of hours depending on the complexity of the forward model and dimensionality of the problem. The added computational efficiency of *Exo Skryer* enables heavier, many parameter, forward models or more computationally demanding physics and chemistry modules to be utilised without increasing the runtime beyond unfeasibility. Large scale model comparison was not performed in

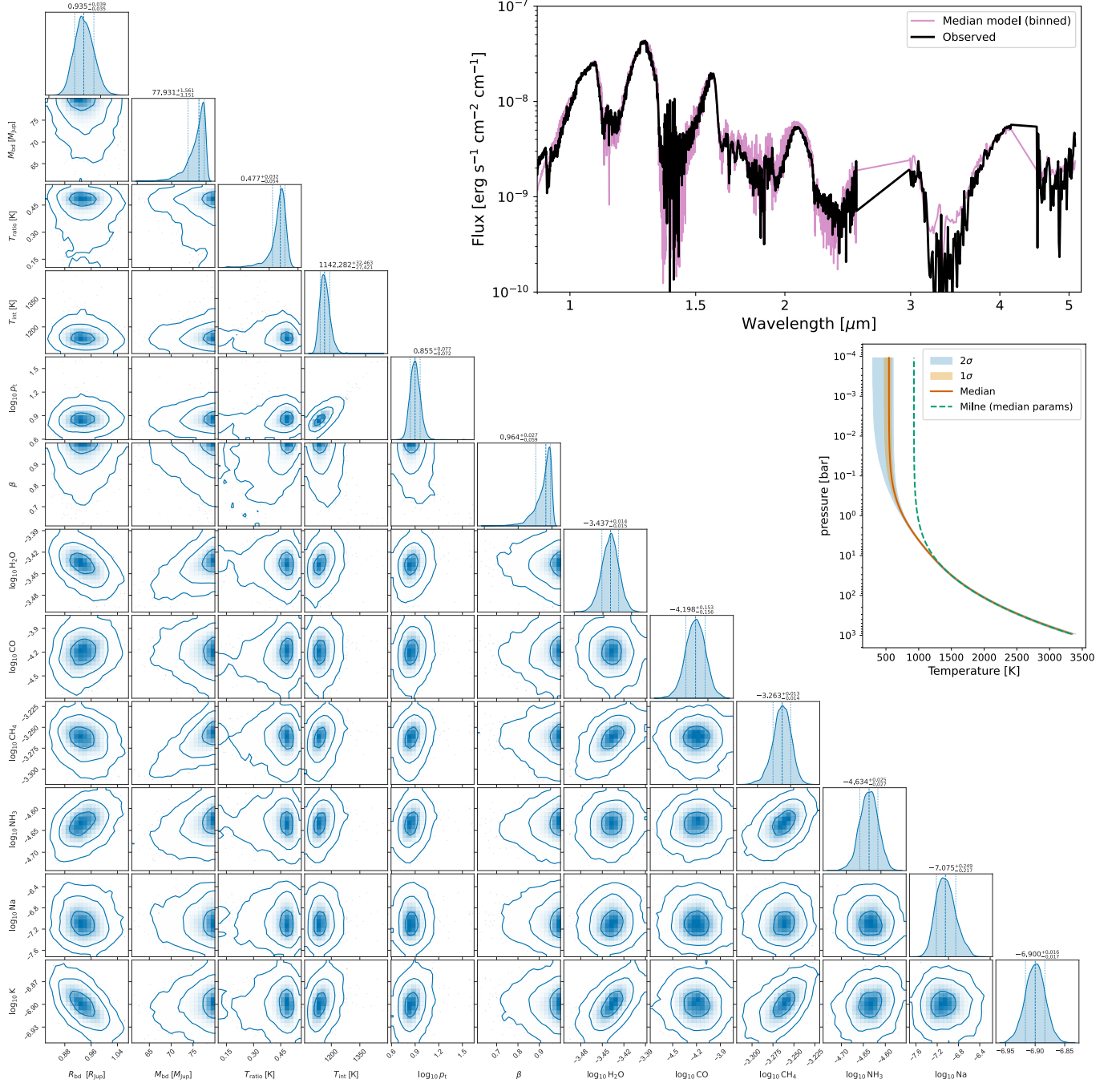


Fig. 9.— Equal weight posterior samples and kernel density estimation for the Gliese 229 B brown dwarf retrieval. The median and  $1\sigma$  confidence intervals are shown as the dashed and dotted lines respectively. The observational data (black) and median best-fit (purple) is shown in the top right panel. The median T-p profile with  $2\sigma$  confidence interval is shown on the right middle panel.

this study, but is foreseen to also be accelerated. Through using a JAX framework, *Exo Skryer* is well placed to integrate current and future machine learning techniques, novel highly parallel sampling methodologies and take advantage of technological developments in GPU hardware.

*Exo Skryer* offers a new microphysical parameter based, cloud opacity retrieval methodology using the mass mixing ratio profile of the cloud as the basic unit of the cloud opacity scheme. This allows retrieval of parameters that can be more directly physically interpreted from cloud microphysical theory. In addition, I presented a new, simple, direct optical con-

stant retrieval methodology for recovering  $(n, k)$  constants for suspected JWST MIRI aerosol absorption bands. These retrievals suggest that the commonly assumed  $\text{SiO}_2$ -quartz composition may not be fully representative of the real material in hot gas giant atmospheres.

Future features *Exo Skryer* include a chemical equilibrium scheme, for example *FastChem* (Stock et al. 2018), and chemical quenching timescale schemes (e.g. Zahnle & Marley 2014). In addition, advanced techniques such as leave-one-out (LOO) methodologies (e.g. Welbanks et al. 2023) to test the sensitivity of Bayesian evidence to specific data points

would be beneficial.

Lastly, the retrievals performed in this study used older, non-optimal hardware, suggesting further speed up of retrieval times than that presented here are possible. This paper acts as the basic reference for *Exo Skryer*, with many updates expected in the future as utilisation increases. *Exo Skryer* is available as open-source software on GitHub<sup>3</sup>.

#### ACKNOWLEDGMENTS

I thank The Open Journal of Astrophysics for providing an accessible peer review outlet for larger, technical papers without publication fees, which are increasingly becoming out of

reach for independent early career scientists. I acknowledge funding from the CSH through the Bernoulli Fellowship. I greatly thank B. Morris for discussions and advice on proper Python package development, JAX and sampling techniques, as well as help with setting up the *Exo Skryer* online documentation drivers. I thank J. Taylor for reading an initial draft of the paper, and providing advice on the retrieval results. I thank D. Kitzmann, L. Welbanks and V. Parmentier for various discussions and advice on retrieval modelling particulars. I thank D. Bower for encouragement and advocacy on the use of JAX for this project.

#### REFERENCES

- Ackerman A. S., Marley M. S., 2001, *ApJ*, 556, 872  
 Al-Refaie A. F., Changeat Q., Waldmann I. P., Tinetti G., 2021, *ApJ*, 917, 37  
 Albert J. G., 2020, arXiv e-prints, arXiv:2012.15286  
 Alderson L. et al., 2022, *MNRAS*, 512, 4185  
 Amundsen D. S., Tremblin P., Manners J., Baraffe I., Mayne N. J., 2017, *A&A*, 598, A97  
 Anderson D. R. et al., 2017, *A&A*, 604, A110  
 Asplund M., Amarsi A. M., Grevesse N., 2021, *A&A*, 653, A141  
 Azzam A. A., Tennyson J., Yurchenko S. N., Naumenko O. V., 2016, *MNRAS*, 460, 4063  
 Barstow J. K., 2020, *MNRAS*, 497, 4183  
 Barstow J. K., Heng K., 2020, *Space Sci. Rev.*, 216, 82  
 Batalha N. E. et al., 2026, *AJ*, 171, 98  
 Benneke B., Seager S., 2012, *ApJ*, 753, 100  
 Blecic J., Dobbs-Dixon I., Greene T., 2017, *ApJ*, 848, 127  
 Bohren C. F., Huffman D. R., 1983, Absorption and scattering of light by small particles  
 Brandt G. M. et al., 2021, *AJ*, 162, 301  
 Buchner J., 2023, *Statistics Surveys*, 17, 169  
 Buchner J. et al., 2014, *A&A*, 564, A125  
 Burningham B., Marley M. S., Line M. R., Lupu R., Visscher C., Morley C. V., Saumon D., Freedman R., 2017, *MNRAS*, 470, 1177  
 Burrows A., Hubbard W. B., Lunine J. I., Liebert J., 2001, *Reviews of Modern Physics*, 73, 719  
 Calamari E. et al., 2022, *ApJ*, 940, 164  
 Changeat Q. et al., 2022, *ApJS*, 260, 3  
 Chubb K. L. et al., 2021, *A&A*, 646, A21  
 Coles P. A., Yurchenko S. N., Tennyson J., 2019, *MNRAS*, 490, 4638  
 Dobbs-Dixon I., Agol E., 2013, *MNRAS*, 435, 3159  
 Dobbs-Dixon I., Blecic J., 2022, *ApJ*, 929, 46  
 Dyrek A. et al., 2024, *Nature*, 625, 51  
 Evans T. M. et al., 2013, *ApJ*, 772, L16  
 Felix L., Kitzmann D., Demory B.-O., Mordasini C., 2025, *A&A*, 701, A296  
 Feng Y. K., Line M. R., Fortney J. J., Stevenson K. B., Bean J., Kreidberg L., Parmentier V., 2016, *ApJ*, 829, 52  
 Fisher C., Heng K., 2018, *MNRAS*, 481, 4698  
 Gandhi S., Brogi M., Webb R. K., 2020, *MNRAS*, 498, 194  
 Grant D. et al., 2023, *ApJ*, 956, L32  
 Grimm S. L., Heng K., 2015, *ApJ*, 808, 182  
 Guillot T., 2010, *A&A*, 520, A27  
 Handley W. J., Hobson M. P., Lasenby A. N., 2015, *MNRAS*, 450, L61  
 Hogan R. J., 2024, *Quarterly Journal of the Royal Meteorological Society*, 150, 318  
 Inglis J. et al., 2024, *ApJ*, 973, L41  
 Irwin P. G. J. et al., 2008, *J. Quant. Spec. Radiat. Transf.*, 109, 1136  
 Irwin P. G. J., Toledo D., Garland R., Teanby N. A., Fletcher L. N., Orton G. A., Bézard B., 2018, *Nature Astronomy*, 2, 420  
 Kawahara H., Kawashima Y., Masuda K., Crossfield I. J. M., Pannier E., van den Bekerom D., 2022, *ApJS*, 258, 31  
 Kawahara H. et al., 2025, *ApJ*, 985, 263  
 Kawashima Y. et al., 2025, *ApJ*, 988, 53  
 Kitzmann D., Heng K., 2018, *MNRAS*, 475, 94  
 Kitzmann D., Heng K., Oreshenko M., Grimm S. L., Apai D., Bowler B. P., Burgasser A. J., Marley M. S., 2020, *ApJ*, 890, 174  
 Kothari H., Cushing M. C., Burningham B., Beiler S. A., Kirkpatrick J. D., Schneider A. C., Mukherjee S., Marley M. S., 2024, *ApJ*, 971, 121  
 Kreidberg L., Line M. R., Thorngren D., Morley C. V., Stevenson K. B., 2018, *ApJ*, 858, L6  
 Kurucz R. L., Bell B., 1995, Atomic line list  
 Lee E. K. H., 2024, *ApJ*, 965, 115  
 Li G., Gordon I. E., Rothman L. S., Tan Y., Hu S.-M., Kassi S., Campargue A., Medvedev E. S., 2015, *ApJS*, 216, 15  
 Line M. R., Parmentier V., 2016, *ApJ*, 820, 78  
 Line M. R., Teske J., Burningham B., Fortney J. J., Marley M. S., 2015, *ApJ*, 807, 183  
 Louie D. R. et al., 2025, *AJ*, 169, 86  
 Lueber A., Kitzmann D., Bowler B. P., Burgasser A. J., Heng K., 2022, *ApJ*, 930, 136  
 MacDonald R. J., 2023, *The Journal of Open Source Software*, 8, 4873  
 MacDonald R. J., Batalha N. E., 2023, *Research Notes of the American Astronomical Society*, 7, 54  
 MacDonald R. J., Lewis N. K., 2022, *ApJ*, 929, 20  
 Madhusudhan N., Seager S., 2009, *ApJ*, 707, 24  
 Mihalas D., 1978, *Stellar atmospheres*  
 Mollière P., Wardenier J. P., van Boekel R., Henning T., Molaverdikhani K., Snellen I. A. G., 2019, *A&A*, 627, A67  
 Moosmüller H., Sorensen C. M., 2018, *J. Quant. Spec. Radiat. Transf.*, 219, 333  
 Moran S. E., Marley M. S., Crossley S. D., 2024, *ApJ*, 973, L3  
 Mullens E., Lewis N. K., MacDonald R. J., 2024, *ApJ*, 977, 105  
 Ohno K., Okuzumi S., 2017, *ApJ*, 835, 261  
 Parmentier V. et al., 2018, *A&A*, 617, A110  
 Phillips M. W. et al., 2020, *A&A*, 637, A38  
 Pinhas A., Rackham B. V., Madhusudhan N., Apai D., 2018, *MNRAS*, 480, 5314  
 Polyansky O. L., Kyuberis A. A., Zobov N. F., Tennyson J., Yurchenko S. N., Lodi L., 2018, *MNRAS*, 480, 2597  
 Prathaban M., Yallup D., Alvey J., Yang M., Templeton W., Handley W., 2025, arXiv e-prints, arXiv:2509.04336  
 Robinson T. D., 2017, *ApJ*, 836, 236  
 Schlawin E. et al., 2024, *AJ*, 168, 104  
 Sing D. K. et al., 2016, *Nature*, 529, 59  
 Sing D. K. et al., 2024, *Nature*, 630, 831  
 Skilling J., 2004, in *American Institute of Physics Conference Series*, Vol. 735, *Bayesian Inference and Maximum Entropy Methods in Science and Engineering: 24th International Workshop on Bayesian Inference and Maximum Entropy Methods in Science and Engineering*, Fischer R., Preuss R., Toussaint U. V., eds., AIP, pp. 395–405  
 Spake J. J. et al., 2018, *Nature*, 557, 68  
 Speagle J. S., 2020, *MNRAS*, 493, 3132  
 Stammes K., Tsay S. C., Jayaweera K., Wiscombe W., 1988, *Appl. Opt.*, 27, 2502  
 Stock J. W., Kitzmann D., Patzer A. B. C., Sedlmayr E., 2018, *MNRAS*, 479, 865  
 Taylor J., Parmentier V., Irwin P. G. J., Aigrain S., Lee E. K. H., Krissansen-Totton J., 2020, *MNRAS*, 493, 4342  
 Toon O. B., McKay C. P., Ackerman T. P., Santhanam K., 1989, *J. Geophys. Res.*, 94, 16287  
 Underwood D. S., Tennyson J., Yurchenko S. N., Huang X., Schwenke D. W., Lee T. J., Clausen S., Fateev A., 2016, *MNRAS*, 459, 3890  
 Wakeford H. R., Sing D. K., 2015, *A&A*, 573, A122  
 Welbanks L. et al., 2024, *Nature*, 630, 836  
 Welbanks L., Madhusudhan N., 2021, *ApJ*, 913, 114  
 Welbanks L., McGill P., Line M., Madhusudhan N., 2023, *AJ*, 165, 112  
 Welbanks L. et al., 2025, *Nature Astronomy*  
 Whitebook S., Brandt T. D., Brandt G. M., Martin E. C., 2024, *ApJ*, 974, L30  
 Wiser L. S. et al., 2025, *Proceedings of the National Academy of Science*, 122, e2416193122  
 Xuan J. W. et al., 2024a, *Nature*, 634, 1070  
 Xuan J. W. et al., 2024b, *ApJ*, 977, L32  
 Yallup D., Kroupa N., Handley W., 2025, in *Frontiers in Probabilistic Inference: Learning meets Sampling*  
 Yurchenko S. N., Mellor T. M., Freedman R. S., Tennyson J., 2020, *MNRAS*, 496, 5282  
 Yurchenko S. N., Owens A., Kefala K., Tennyson J., 2024, *MNRAS*, 528, 3719  
 Zahnle K. J., Marley M. S., 2014, *ApJ*, 797, 41  
 Zalesky J. A., Line M. R., Schneider A. C., Patience J., 2019, *ApJ*, 877, 24  
 Zeidler S., Posch T., Mutschke H., 2013, *A&A*, 553, A81  
 Zhang M., Paragas K., Bean J. L., Yeung J., Chachan Y., Greene T. P., Lunine J., Deming D., 2025, *AJ*, 169, 38

<sup>3</sup> <https://github.com/ELeeAstro/Exo.Skryer>

## APPENDIX

## A. WASP-107B WITHOUT MIRI

This paper was built using the Open Journal of Astrophysics  $\LaTeX$  template. The OJA is a journal which provides fast and easy peer review for new papers in the `astro-ph` section of the arXiv, making the reviewing process simpler for authors and referees alike. Learn more at <http://astro.theoj.org>.

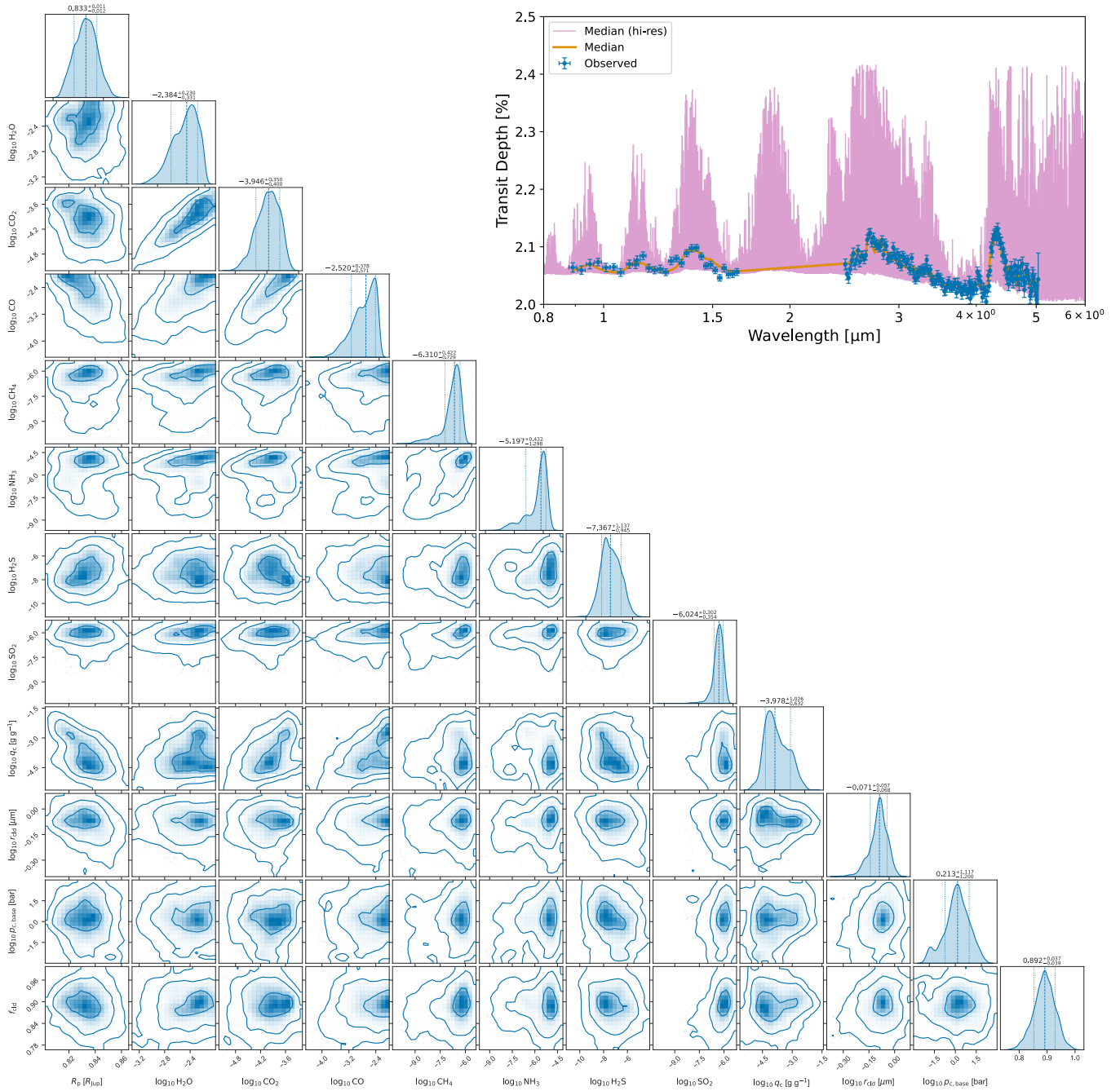


FIG. 10.— Equal weight posterior samples and kernel density estimation for the WASP-107b retrieval, but without the inclusion of the MIRI data. The median and  $1\sigma$  confidence intervals are shown as the dashed and dotted lines respectively. The observational data (blue) and median best-fit (purple) is shown in the top right panel.